

OPEN ACCESS

Editors' Choice—Capacity Fading Mechanisms of NCM-811 Cathodes in Lithium-Ion Batteries Studied by X-ray Diffraction and Other Diagnostics

To cite this article: Franziska Friedrich *et al* 2019 *J. Electrochem. Soc.* **166** A3760

View the [article online](#) for updates and enhancements.



Capacity Fading Mechanisms of NCM-811 Cathodes in Lithium-Ion Batteries Studied by X-ray Diffraction and Other Diagnostics

Franziska Friedrich,^{1,*,*,z} Benjamin Strehle,^{1,*,*} Anna T. S. Freiberg,^{1,*} Karin Kleiner,^{1,2} Sarah J. Day,² Christoph Erk,³ Michele Piana,^{1,**} and Hubert A. Gasteiger^{1,***}

¹Chair of Technical Electrochemistry, Department of Chemistry and Catalysis Research Center, Technical University of Munich, D-85748 Garching, Germany

²Harwell Science and Innovation Campus, Diamond Light Source, Didcot, Oxfordshire OX11 0DE, UK

³BASF SE Ludwigshafen, Lithium-Ion Battery Research, D-67056 Ludwigshafen, Germany

Ni-rich layered oxides, like NCM-811, are promising lithium-ion battery cathode materials for applications such as electric vehicles. However, pronounced capacity fading, especially at high voltages, still lead to a limited cycle life, whereby the underlying degradation mechanisms, e.g. whether they are detrimental reactions in the bulk or at the surface, are still controversially discussed. Here, we investigate the capacity fading of NCM-811/graphite full-cells over 1000 cycles by a combination of in situ synchrotron X-ray powder diffraction, impedance spectroscopy, and X-ray photoelectron spectroscopy. In order to focus on the NCM-811 material, we excluded Li loss at the anode by pre-lithiating the graphite. We were able to find a quantitative correlation between NCM-811 lattice parameters and capacity fading. Our results prove that there are no considerable changes in the bulk structure, which could be responsible for the observed $\approx 20\%$ capacity loss over the 1000 cycles. However, we identified the formation of a resistive surface layer, which is responsible for (i) an irreversible loss of capacity due to the material loss for its formation, and (ii) for a considerable impedance growth. Further evidence is provided that the surface layer is gradually formed around the primary NCM-811 particles.

© The Author(s) 2019. Published by ECS. This is an open access article distributed under the terms of the Creative Commons Attribution Non-Commercial No Derivatives 4.0 License (CC BY-NC-ND, <http://creativecommons.org/licenses/by-nc-nd/4.0/>), which permits non-commercial reuse, distribution, and reproduction in any medium, provided the original work is not changed in any way and is properly cited. For permission for commercial reuse, please email: oa@electrochem.org. [DOI: 10.1149/2.0821915jes]



Manuscript submitted September 3, 2019; revised manuscript received October 23, 2019. Published November 14, 2019. This was Paper 559 presented at the Dallas, Texas, Meeting of the Society, May 26–May 30, 2019.

Introduced by Sony in 1991, lithium-ion batteries (LIB) now dominate the battery market. However, a large-scale commercialization of battery electric vehicles (BEVs) and storage systems for renewable energy sources requires higher energy density, lower price, and longer cycle life, all of which critically depend on the cathode active material (CAM). Layered transition-metal oxides (LiTMO₂, where TM refers to one or a combination of the transition-metals (TMs) Ni, Co, and/or Mn, so-called NCMs) have been successfully used as CAMs in LIBs owing to their high specific capacity and high thermal stability. For example, the currently sold BMW i3 BEV uses NCM-111, which is expected to be replaced by NCM-622 in the near future in order to increase energy density and to reduce the cobalt content,¹ as the latter is problematic from a sustainability and geopolitical point of view.^{2–4} For these reasons, the more Ni-rich NCM variants (e.g., NCM-811) are the most promising candidates for future BEV applications, particularly as a higher Ni content leads to an increase in specific capacity at a given cut-off voltage compared to the less Ni-rich NCMs. However, large amounts of Ni in the CAM result in reduced structural, cycling and thermal stability.^{5–7} Especially at high potentials (>4 V vs. Li⁺/Li), structural instabilities such as bulk structural transformations^{6,8–10} and cation disorder (anti-site disorder between lithium and a transition-metal)¹¹ are reported to deteriorate the electrochemical performance of layered oxides. Some authors identified micro-strain and intergranular cracking as major causes for capacity fading in Ni-rich NCMs.^{12–14}

Other research activities focus on the structural evolution of the CAM surface, because it happens simultaneously with electrochemical cycling and determines the interaction between active material and the other components of the battery. Recent on-line electrochemical mass spectrometry (OEMS) and transmission electron microscopy (TEM) studies on NCMs and their over-lithiated variants (referred to as HE-

NCMs) report oxygen release at the particle surface^{15–18} accompanied by the formation of rock-salt and spinel-type surface layers.^{17–20} The low conductivity of these reconstructed phases is believed to cause an increased impedance on the cathode side and therefore contribute considerably to the capacity loss.^{18,20} Furthermore, the literature reports that transition-metal dissolution from the CAM deteriorates cycling performance in NCM/graphite full-cells. While on the cathode side active material is lost and the particle surface is reconstructed, the deposition of dissolved transition-metals on the anode side leads to enhanced electrolyte decomposition and an impedance rise.^{21–23}

In view of the required lifetime of 15 years and a cycle life over 1000 cycles for large-scale commercialization of LIBs for applications such as electric vehicles,^{24,25} it is essential to gain a fundamental understanding of the underlying mechanisms and their interrelations contributing to battery failure. As ex situ techniques may lead to deviations from the original state of the CAMs during electrode harvesting (e.g., changes in the state-of-charge (SOC) of the CAMs), much more authoritative information can be achieved by in situ and operando techniques, which allow for the characterization of electrode materials under real operating conditions. In situ X-ray powder diffraction (XPD) is a powerful analytical tool, which provides insights about bulk structural changes in cathode and anode over the course of cycling.

In the present study, detailed information on the fading mechanisms of NCM-811/graphite full-cells is obtained from the combination of X-ray powder diffraction, electrochemical impedance spectroscopy (EIS), rate tests, X-ray photoelectron spectroscopy (XPS) and scanning electron microscopy (SEM). To get unambiguous insights about the cathode active material fading mechanisms, the graphite counter-electrode was pre-lithiated to eliminate capacity fading from active lithium loss at the anode, while allowing for long-term cycling which is more problematic with a metallic lithium anode. In situ synchrotron X-ray powder diffraction experiments were conducted with pouch cells cycled over 1000 times at the long duration experiment (LDE) facility of beamline I11 at the Diamond Light Source, UK. The results from the LDE synchrotron XPD study were combined with operando XPD measurements using a lab diffractometer with a molybdenum

^zThese authors contributed equally to this work.

*Electrochemical Society Student Member.

**Electrochemical Society Member.

***Electrochemical Society Fellow.

^zE-mail: franziska.friedrich@tum.de

source to allow for a quantitative correlation between lattice parameter changes in the CAM and capacity losses, seeking to clarify whether bulk or surface related phenomena are responsible for capacity fading in NCM-811 CAMs.

Experimental

Battery assembly and cycling.—NCM-811 cathode electrode sheets (94 wt% BASF SE NCM-811, 2 wt% Timcal SFG6L graphite, 1 wt% Timcal C65 conductive carbon, 3 wt% Kynar PVDF binder HSV900) with a loading of ≈ 7.4 mg_{CAM}/cm² (corresponding to ≈ 1.5 mAh/cm² based on 200 mAh/g) and with a precise composition of Li_{1.01}Ni_{0.79}Co_{0.1}Mn_{0.1}O₂ (Mikroanalytisches Labor Pascher, Germany; see below) were provided by BASF SE (Germany). The pristine NCM-811 has a BET surface of ≈ 0.27 m²/g (determined by N₂ and Kr physisorption; see below). Cathodes with a geometric area of 9 cm² (30 × 30 mm²) were assembled in single layer pouch cells (with a 40 μm-thick Al layer) versus graphite counter-electrodes (CE, geometrically oversized, 33 × 33 mm²) in an argon-filled glove box (<0.1 ppm O₂ and H₂O, MBraun, Germany). These capacitively oversized graphite sheets (96 wt% active material, ≈ 7.1 mg_{Graphite}/cm², reversible capacity of ≈ 2.3 mAh/cm²) were also provided by BASF SE. To avoid capacity fading due to the loss of cyclable lithium caused by the formation of the solid electrolyte interphase (SEI) as well as during cycling, the graphite anodes were pre-lithiated to \approx Li_{0.3}C₆ (corresponding to ≈ 0.7 mAh/cm²) versus a lithium counter-electrode (450 μm, 99.9%, Rockwood Lithium) in LP57-2 electrolyte (1M LiPF₆ in EC:EMC = 3:7 by weight with 2% VC, BASF SE). In full-cells, two glass-fiber (GF) separators (36 × 36 mm², glass microfiber filter 691, VWR, Germany) with a projecting tab (10 × 10 mm²) were used with 700 μL LP57-2 electrolyte. A piece of lithium (10 × 5 mm²) positioned at the tab, was used as reference-electrode (RE). For a homogeneous compression of the cells at ≈ 2 bar, a homemade spring-loaded pouch cell holder with a 1.5 mm diameter hole as X-ray window was used, similar to that reported in our previous work.²⁶

The first two formation cycles were performed at constant current (CC) at a C-rate of C/10 (based on 200 mAh/g, which corresponds to a current density of ≈ 1.5 mA/cm² at a rate of 1C). Subsequent CC cycling was carried out at C/2 (without any constant voltage hold step). The cathode voltage window was 3.0–4.5 V vs. Li⁺/Li as controlled versus the Li-RE. All voltages in this work are reported vs. Li⁺/Li if not stated otherwise. Initial cycling (2 cycles at C/10 and 6 cycles at C/2) was performed at the Technical University of Munich (Maccor cyler, series 4000, USA) in a thermostatic chamber at 25°C. At the long duration experiments (LDE) facility of beamline I11 at the Diamond Light Source, two nominally identical pouch cells were cycled at C/2 and $\approx 22^\circ\text{C}$. The following nomenclature will be used: (i) “pristine” refers to the as-received NCM-811 powder or to pristine electrode sheets (i.e., never assembled into a battery); (ii) “fresh” corresponds to data collected within the first 10 cycles (including formation cycles); (iii) “begin-of-test” (BOT) refers to a NCM-811 cathode electrode, which has gone through formation (initial 2 cycles at C/10) and 16 cycles at C/2, corresponding to our first LDE XPD data point; and, (iv) “end-of-test” (EOT) refers to a cathode at the end of the LDE test, more specifically, it refers to the LDE XPD data collected in cycle 968 for cell 1 and in cycle 975 for cell 2, although the electrochemical cycling continued until cycle 995 for cell 1 and cycle 1003 for cell 2. Subsequently, further tests were conducted (e.g., C-rate test, relaxation test), which are also denominated as EOT.

For elemental analysis, inductively coupled plasma atomic emission spectroscopy (ICP-AES) was performed at the Mikroanalytisches Labor Pascher (Remagen, Germany), for which the CAM powder was dissolved by pressurized acid digestion in aqua regia. Considering surface impurities such as Li₂SO₄, Li₂CO₃, and transition-metal carbonates, which amount in total to ≈ 2.2 wt% of the sample, the composition of NCM-811 was determined as Li_{1.01}Ni_{0.79}Co_{0.10}Mn_{0.10}O₂, giving a theoretical capacity of 280 mAh/g_{NCM} or 274 mAh/g_{CAM} (including the surface impurities) for complete Li extraction. Note that capacity values are given for the total CAM powder and that we used

the latter notation throughout the entire work. The layered oxide is doped with ≈ 0.3 mol% Al (relative to the transition-metal amount), which is however not taken into further consideration.

X-ray powder diffraction measurements.—The in situ long-duration study of two nominally identical NCM-811/graphite pouch cells was performed using synchrotron X-ray powder diffraction on the LDE facility of beamline I11, Diamond Light Source; this will further on be referred to as “in situ S-XPD”. Patterns were collected with an exposure time of 5 minutes with an X-ray beam of ≈ 25 keV energy (≈ 0.494 Å) and a 2D Pixium area detector at a distance of ≈ 0.25 m. NIST Standard Reference Material CeO₂ (NIST SRM 674b) was measured before every sample data collection in order to refine the wavelength and detector distance and to evaluate the instrumental broadening. Detailed information on the LDE instrument is given by Murray et al.²⁷ The diffraction data were reduced with the software package DAWN^{28,29} and refined with the software package Topas (version 6).³⁰ XPD data collection was performed once a week at open circuit voltage (OCV) after 3–5 h of relaxation, both in the discharged state of the cathode at the lower cathode cut-off potential of 3.0 V vs. Li⁺/Li and, after subsequent charging, in the charged state of the cathode at the upper cathode cut-off potential of 4.5 V vs. Li⁺/Li. In this way, data collection was intended to be performed every ≈ 50 cycles at both SOC. However, due to a beam shut-down no XPD data could be collected for several months. The cycling protocol was nevertheless continued including OCV holds every week (i.e., every ≈ 50 cycles).

In addition, XPD experiments were conducted at our in-house STOE STADI P diffractometer (STOE, Germany) in transmission mode using Mo-K_{α1} radiation (0.7093 Å, 50 kV, 40 mA) and a Mythen 1K detector with one data point every 0.015°/2θ. For the determination of instrumental broadening, a silicon standard material (NIST SRM 640c) was used. In-house measurements comprise three different types of experiments for the pristine, fresh, and harvested EOT NCM-811 materials: (i) structural information from ex situ capillary data; (ii) determination of lattice parameters and of a calibration curve correlating the lithium content x_{Li} with the *c/a* lattice parameter ratio ($x_{\text{Li}} = f(c/a)$), which was performed both in operando (i.e., data collection during charge-discharge cycling) and in situ mode (i.e., data collection during intermediate OCV holds), and, (iii) relaxation tests of the (003) reflection upon the transition from CC charge to OCV. XPD experiments conducted with the Mo-K_{α1} laboratory XPD will further on be referred to as “L-XPD” experiments.

Ex situ L-XPD measurements were conducted over night (≈ 14 h) in 0.3 mm borosilicate capillaries in a 2θ range of 3–60° (with detector step size/step time of 0.15°/5 s). Cycled samples were scratched off the electrode and filled into the capillary in an argon-filled glove box.

In situ and operando L-XPD experiments were performed in pouch cells with a lithium counter-electrode and a relatively thin pouch foil (12 μm-thick Al layer). During the measurement, the cell was connected to a SP200 potentiostat (SP200, Biologic, France). For the determination of lattice parameters from the fresh NCM-811 electrode, all cycles were conducted at a C-rate of C/7.5. The first charge was limited to a maximum capacity of 180 mAh/g (corresponding to a cathode potential of ≈ 4.1 V vs. Li⁺/Li) to avoid any side reactions of the electrolyte. By limiting the SOC window and using a Li counter-electrode, the observed irreversible capacity loss could be solely related to the NCM-811 CAM. Afterwards, the cell was cycled for several cycles at C/7.5 between cathode potentials of 3.0 and 4.6 V vs. Li⁺/Li; the accumulated irreversible capacity loss caused by side reactions amounted to ≈ 9 mAh/g during the operando measurement, and the SOC scale in the respective figures was corrected for this value. The *c/a* ratio was measured operando at C/7.5 with a time resolution of 8 minutes (see below), translating to one diffractogram every ≈ 4 mAh/g; for in situ measurements (i.e., during a 50 min OCV hold), diffractograms were taken every 10 mAh/g. The EOT sample was cycled in situ using the cycling protocol for the LDE experiment (i.e., at C/2 between 3.0 and 4.5 V vs. Li⁺/Li) with data points every 15 mAh/g. In situ L-XPD data collection was performed during intermittent OCV periods in the cycling procedure in a 2θ range of 6–48° (detector step size/step time

of 0.15°/5 s), leading to L-XPD acquisition times of 40 minutes. For operando L-XPD data collection, only small 2θ sections with non-overlapping NCM reflections were measured in repetition mode. To determine the c/a calibration curve from operando L-XPD, the (003) reflection was monitored in the 2θ range of 8.000–9.215° (0.405°/3 s), and the (110) reflection in the 2θ range of 28.500–29.715° (0.405°/3 s), with an overall acquisition time of about 8 minutes. Lattice parameter values determined by the operando L-XPD method perfectly overlap with those from in situ L-XPD data (see Figure S5 in paragraph S3 of the Supporting Information), whereby the operando method has the advantage that more data points are collected.

Finally, additional operando L-XPD lattice parameter relaxation experiments were conducted with fresh and EOT samples. After C/2 charging to a comparable state of delithiation (i.e., cathode potential cut-offs of 4.3 V vs. Li^+/Li for the fresh and of 4.5 V vs. Li^+/Li for the EOT sample), the cell was allowed to relax at OCV while monitoring only the relaxation of the (003) reflections in the 2θ range of 8.000–9.215° (0.405°/3 s), resulting in a time resolution of about 4 minutes per L-XPD pattern.

Rietveld refinement.—As the X-ray beam penetrates through the entire pouch cell, the synchrotron diffractogram contains reflections of (i) Al from the pouch foil and the cathode current collector, (ii) Cu from the anode current collector, (iii) graphite phases (graphite as conductive agent in the cathode, Li_xC_6 in the anode), and, (iv) the actual NCM reflections of interest. The scattering from the electrolyte-soaked separator and from polymers of the binder and pouch cell give rise to a complex background, which was fitted by different approaches. Initially, the background signal was defined by fitting a linear interpolation between selected data points in non-overlapping regions, as was done by Dolotko et al.³¹ However, a more elegant way – because its inclusion in the refinement process is possible – is a user-defined background modeled by eight pseudo-Voigt peaks, similar to what was used by Bo et al.,³² and which was used throughout our analysis. From the refinement of one pattern, the positions and relative intensities of the pseudo-Voigt peaks were determined and fixed across all scans with a single scale factor allowing for a free variation of the overall background intensity. Due to preferred orientation effects in the metal foils, a structure-independent Pawley fit was used for the respective phases. The peak profile was described as isotropic broadening with the Thompson-Cox-Hastings pseudo-Voigt function (TCHZ, as implemented into Topas). The instrumental contribution to the broadening was determined with the CeO_2 standard (NIST SRM 674b), giving a value of ≈ 0.006 for the θ -independent parameter W in the TCHZ function. Additional isotropic reflection broadening caused by the sample was taken into account as phase-specific micro-strain ($\tan \theta$ -dependent parameter X) or crystallite size effects ($1/\cos \theta$ -dependent parameter Y) in the TCHZ function of each individual phase. For a more detailed discussion see paragraph S1 in the SI.

NCM-811 is a layered transition-metal oxide known to exhibit an α - NaFeO_2 -type structure with $R\bar{3}m$ symmetry.³³ The unit cell of NCM-811 contains Li atoms on the 3a site (fractional coordinates: 0, 0, 0) and the transition-metals randomly distributed on the 3b site (0, 0, 1/2). The oxygen atoms are on the 6c site (0, 0, $z_{6c,O}$), with $z_{6c,O}$ ranging between 0.23 and 0.24. According to literature reports³⁴ and our own experience, a more stable refinement is achieved if the number of refined parameters is minimized. Therefore, the following constraints were applied: (i) the site occupancy factors of Co and Mn were both fixed to 0.10 on the 3b site (as determined from the ICP-AES analysis); (ii) the overall Ni content was fixed to 0.79 per formula unit; and, (iii) for the refinement of cation disorder, the Ni distribution between 3a and 3b sites was constrained by assuming the same amount of Li on the transition-metal 3b site as the amount of Ni on the Li 3a site (\equiv Li-Ni mixing, cation disorder). The chosen kind of constraints have already been applied in the literature and were found to give chemically reliable results and a stable refinement.^{10,31,35–38} Furthermore, the atomic displacement parameter was constrained for all sites to be the same, because otherwise physically meaningless (sometimes negative) values were obtained. However, when refining data obtained from ex situ

L-XPD capillary measurements, site-specific atomic displacement parameters could be implemented, which were in good agreement with literature values.^{39,40} We used ionic scattering factors for all atoms in the structure. Generally, there is no commonly accepted rule whether to use ionic or neutral atomic form factors.⁴¹ However, recently the advantages of the use of composite structure factors were reported.³⁴

At this point, it is important to note that structure factors are a (theoretical) model of the electron density of an atom which scatters X-rays. Usually, a scattering factor of a free neutral atom deviates substantially from that of an atom in a crystal lattice. However, full charge-transfer between atoms rarely occurs, so that the actual charge density of an ion in a crystal lattice is not equal to its formal charge.^{34,42,43} Accurate scattering factors therefore need to be determined for the respective structural model. As such data are not available for NCM-811, the scattering factors were chosen so that the resulting oxidation states (Li^+ , Ni^{3+} , Co^{2+} , Mn^{4+} , and O^{2-}) give a chemically meaningful, neutral sum formula for the pristine material. The effects of the scattering factors might be mitigated by excluding the low 2θ region from the Rietveld refinement.³⁴ In our case, however, this is not possible because strong reflections are in this range and discarding them would mean a detrimental loss of information.

Any anisotropic strain introduced by changes in the lattice due to Li de-/intercalation (especially pronounced at high state-of-charge, SOC) was taken into account by the hexagonal Stephens model (see paragraph S1 in the SI for equations and Figure S3 for the Williamson-Hall plot).⁴⁴ The simultaneous refinement of the four micro-strain parameters (S_{004} , S_{004} , S_{202} , S_{301}) during the sequential Rietveld analysis of the LDE pouch cell data did not yield stable results. Therefore, only S_{004} and S_{202} were used, because these parameters had the largest effect on the fit quality. This procedure is in agreement with the literature.⁴⁵ For the refinement of the capillary data measured at the in-house diffractometer, all four strain parameters were used successfully, underlining the fact that the Stephens model is phenomenological and only helps to describe the peak shape but does not directly correspond to a physical meaning. In case of the refinement of capillary data obtained at the in-house diffractometer, absorption correction was applied. For further details on the structural parameters, constraints, and refinement results see paragraphs S1 and S2 in the SI.

In addition to the NCM phase, graphite phases of the anode were observed in the XPD patterns from NCM-811/graphite full-cells. It is known in the literature^{31,46} that the lithiation of graphite is a step-wise process leading to three phases which are distinguishable by X-ray diffraction analysis: graphite (space group $P6_3/mmc$), LiC_{12} ($P6/mmm$), and LiC_6 ($P6/mmc$). The pre-lithiation of the anode results in a lithium reservoir which ensures that even in the fully discharged cell, graphite is not formed. The nevertheless observed (002) graphite reflection therefore stems from the conductive graphite additive in the NCM-811 cathode coating. Structural parameters for the refinement of the Li_xC_6 phases ($0 < x < 1$) were taken from a neutron study conducted by Dolotko et al.⁴⁷ As just the small (002) reflection of graphite appears, only the lattice parameters were refined for this phase. For the LiC_{12} phase, lattice parameters and peak broadening due to size effects could be refined. At high SOC, also LiC_6 is present, from which the lattice parameters and crystallite size broadening could be refined. Results from the structural refinement of the LDE data with respect to the different graphite phases are shown in Tables S7–S9 in the SI.

Impedance measurements and rate tests.—Electrochemical impedance spectroscopy (EIS) experiments were conducted in spring-compressed Swagelok-type T-cells (≈ 1 bar), in which both cathode and anode had a diameter of 11 mm. Pre-lithiated graphite was used as counter-electrode. A gold wire micro-reference (GWRE) with a Au wire diameter of 50 μm insulated with a 7 μm polyimide shrouding (Goodfellow Ltd., UK) was used as reference-electrode,⁴⁸ placed between two GF separators with 60 μL LP57-2 electrolyte. The GWRE was lithiated with a constant current of 150 nA for 1 h and yielded a constant potential of 0.31 V vs. Li^+/Li . Potential-controlled electrochemical impedance measurements (PEIS) were conducted with a potentiostat (VMP300, BioLogic, France) in a frequency range of

100 kHz to 100 mHz with an AC voltage perturbation of 10 mV (taking 20 data points per decade and 3 period repetitions). PEIS measurements were performed during the first formation cycle, the 18th cycle, and at end-of-test during charge and discharge at intervals of 20 mAh/g. Prior to measurements, the cells were allowed to rest at OCV for 1 h. Harvested cathode material from the pouch cells of the LDE study was used for the PEIS experiments and for rate tests at EOT. For the other two cycles of interest, new cells were assembled. To fit the impedance spectra, the transmission line model (TLM) was used as described in paragraph S4 of the Supporting Information.⁴⁹

Rate tests were done in 2325-type coin cells with cathode electrodes of 11 mm (EOT) and 14 mm (BOT) in diameter, a lithium counter-electrode (15 mm), two GF separators (16 mm), and 80 μ L LP57 electrolyte (1M LiPF₆ in EC:EMC = 3:7 by weight, BASF SE).

X-ray photoelectron spectroscopy measurements.—X-ray photoelectron spectroscopy (XPS) measurements were conducted on pristine, BOT, and EOT electrode samples with focus on the O1s region. The electrodes were used as-received (pristine) or harvested without washing in the completely discharged state (i.e., after a constant voltage hold step at 3.0 V vs. Li⁺/Li until a C/100 current cut-off). 4 mm diameter samples were cut out of the electrode sheets inside an argon-filled glove box (<0.1 ppm O₂ and H₂O, MBraun, Germany), mounted floating onto a stainless steel stub, and transferred into the loadlock of the XPS system without air exposure using the transfer device from Kratos (UK). XPS spectra were recorded with a monochromatic Al K _{α} source (1486.6 eV), using an Axis Supra system (Kratos, UK) with an operating pressure of 2·10⁻⁸ Torr. A pass energy of 20 eV, step size of 0.1 eV and dwell time of 200 ms were chosen for a spot size of 800 × 300 μ m². Binding energies were corrected based on the adventitious carbon signal at 284.8 eV in the C 1s spectrum. Fitting of the spectra was done with a mixture of Lorentzian (30%) and Gaussian (70%) shape function on top of a Shirley background.

Surface area determination.—Surface area measurements were performed on a gas sorption analyzer (Autosorb-iQ, Quantachrome, USA) at 77 K using either nitrogen or krypton as adsorbent. Beforehand, the pristine NCM-811 powder was degassed at 350°C for 3 h, whereas treated powders were degassed at 80°C for 24 h. The CAM

was either treated with (i) H₂O for 30 min or (ii) LP57 + 1000 ppm H₂O for 7 days, whereby in the latter case, previous work showed that the 1000 ppm H₂O will be converted to \approx 2000 ppm HF within the course of roughly 2–3 days.⁵⁰ The CAM-to-solvent ratio was 1:10 g:ml in both cases. Afterwards, the CAM was filtrated and additionally washed with dimethyl carbonate for the HF-treated sample. The specific surface area was determined from adsorption isotherms in the relative pressure range of 0.05 < p/p₀ < 0.30 according to the Brunauer-Emmet-Teller (BET) theory. As N₂ and Kr sorption provide similar surface areas for the pristine material (N₂: 0.26 m²/g, Kr: 0.28 m²/g), the following experiments were only done with krypton, since it should be more accurate with a low sample amount (\approx 1 g).

Overview.—Figure 1 summarizes the main techniques which we have used in this study and which will be discussed in detail in the Results and Discussion section. It might be helpful for the reader to go back to this overview from time to time, especially with respect to the different XPD techniques, as it shows the targeted parameter(s) of each experiment and the different aging states of the NCM-811 CAM.

Results and Discussion

LDE electrochemical data.—Figure 2a shows the specific discharge capacity of two NCM-811/graphite full-cells cycled at the long duration experiment (LDE) facility of beamline I11 at the Diamond Light Source, UK. Initially, there is a first cycle irreversible capacity loss (ICL) of \approx 25 mAh/g (not shown), which compares well with the ICL reported for NCM-111 of \approx 24 mAh/g⁵¹ and which results in a CAM stoichiometry of Li_{0.92}Ni_{0.79}Co_{0.10}Mn_{0.10}O₂ after the first cycle. This irreversible capacity loss of NCMs was also reported by other groups,^{51–55} and Buchberger et al.⁵¹ discussed various reasons for the ICL and were able to prove the mechanism first proposed by Kang et al.,^{54,55} who suggested that the Li diffusion at the end of discharge is very sluggish because of the lack of Li-ion vacancies. These authors were able to recover the full capacity by giving the diffusion process enough time at voltages lower than 3.0 V. The capacity drops after the second cycle by \approx 16 mAh/g when increasing the C-rate from C/10 to C/2 (see inset of Figure 2a), a typical rate-induced capacity loss observed for NCMs.⁵⁶ In addition, between cycle 8 and 9 there

Technique	Target	Figure	Pristine CAM powder	Fresh <10 cycles	BOT Cycle 18	LDE Cycling	EOT \approx 1000 cycles
In situ S-XPD	$\Delta C_{\text{Material}}$ & $\Delta C_{\text{Overpotential}}$	Fig. 5			✓	✓	✓
Operando L-XPD	$c/a = f(x_{\text{Li}})$	Fig. 5a		✓			
In situ L-XPD	$c/a = f(\text{OCV})$	Fig. 6a		✓			✓
Ex situ L-XPD	Li-Ni mixing	Fig. 3	✓				✓
Operando L-XPD	Relaxation	Fig. 9		✓			✓
In situ EIS	R_{CT}	Fig. 6b		✓	✓		✓
Rate test	$\Delta C_{\text{Material}}$	Fig. 7			✓		✓
XPS	Nature of surface layer	Fig. 8	✓		✓		✓

Figure 1. Overview of the main techniques used in this work, highlighting the targeted parameter(s), the figure where the respective results are shown in the Results and Discussion section, and the different aging states of the NCM-811 CAM which have been investigated with the respective technique.

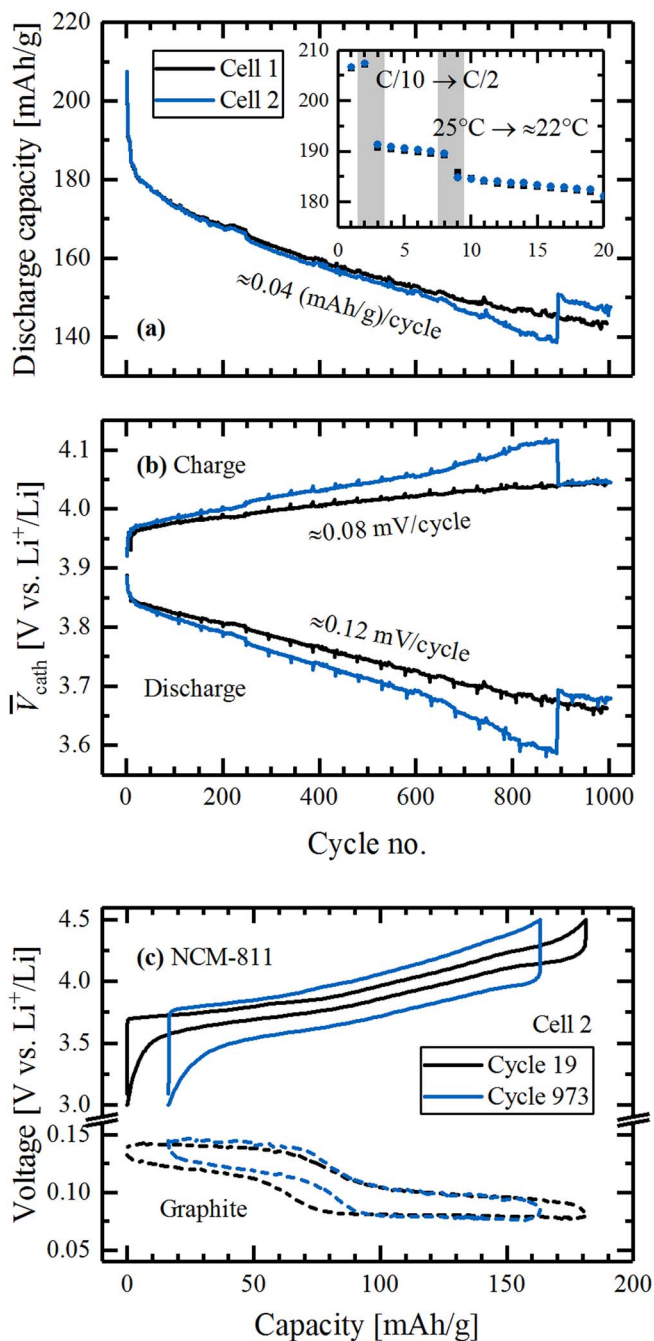


Figure 2. (a) Specific discharge capacity, (b) charge-averaged mean charge and discharge voltage of the cathode vs. Li^+/Li (\bar{V}_{cath}), and (c) voltage profile of anode and cathode of NCM-811/graphite full-cells cycled at $\approx 22^\circ\text{C}$ with C/2 between 3.0–4.5 V vs. Li^+/Li at beamline I11 (Diamond Light Source, UK). The inset in panel (a) highlights the first 20 cycles, where (i) the C-rate was increased from C/10 (cycles 1 and 2) to C/2, and (ii) the cells were moved to the Diamond Light Source (between cycle 8 and 9), where the cycling temperature was $\approx 22^\circ\text{C}$ compared to 25°C during cycles 1–8. Slight deviations from the characteristic mean voltage curves in panel (b) originate from the OCV phases for XPD data collection (every ≈ 50 cycles). The half-cell voltage profiles of cycle 973 in panel (c) were shifted arbitrarily along the x-axis relative to cycle 19 in order to illustrate the overpotential leading to capacity fading.

is another capacity drop of $\approx 3\text{--}5$ mAh/g at the same C-rate, which unfortunately is due to a temperature difference between the cycling experiments conducted in our laboratory at the Technical University Munich (25°C , until cycle 8) and in the beamline hutch at the Diamond Light Source ($\approx 22^\circ\text{C}$, from cycle 9 onwards). This difference

in discharge capacity is consistent with the temperature dependence of the discharge capacity of ≈ 0.8 (mAh/g)/K, determined in a separate experiment (not shown) with fresh NCM-811/graphite cells cycled at C/2 at varying temperatures ($19\text{--}33^\circ\text{C}$). The mean capacity drop in the subsequent cycles is ≈ 0.04 mAh/g per cycle (see Figure 2a), resulting in a capacity retention (at 22°C and C/2) of 77–80% after 1000 cycles, referenced to 185 mAh/g in cycle 9. The instantaneous regain of capacity for cell 2 (blue line) in cycle 893 must have been caused by a sudden improvement of the cell contact (i.e., the electrical contact between the current collector tab of the cell and the crocodile clamp of the current cable). This becomes apparent from the voltage profiles of cell 2 in cycles 892–894, which show a ≈ 100 mV lower charge and discharge voltage after the event in cycle 893 (corresponding to a $\approx 15\ \Omega$ lower resistance; see paragraph S5 and Figure S8 in the SI). However, the capacity fading rate after this event remains unchanged for the subsequent cycles.

Figure 2b shows the charge-averaged mean charge and discharge voltage of the cathode electrodes vs. Li^+/Li of cells 1 and 2 (for a given charge or discharge cycle, $\bar{V}_{\text{cath}} \equiv \int V_{\text{cath}} \times dq / \int dq$).⁵⁷ After the initial rapid increase of \bar{V}_{cath} due to the increase in C-rate (from C/10 to C/2 in the 3rd cycle) and change in temperature (from 25°C to $\approx 22^\circ\text{C}$ in cycle 9), the \bar{V}_{cath} curves for charge and discharge show a relatively linear behavior, with the mean discharge voltage decreasing by ≈ 0.12 mV per cycle and the mean charge voltage increasing by ≈ 0.08 mV per cycle. The increase of the overpotential during both charge and discharge suggests an increase in cathode impedance over extended cycling. The small spikes in the \bar{V}_{cath} curves every ≈ 50 cycles are caused by the OCV holds for XPD data collection, where the cell potential relaxes. The \bar{V}_{cath} jump of cell 2 at cycle 893 is due to the above discussed change in the cell contact resistance.

Figure 2c shows a comparison of the half-cell voltage profiles of graphite and NCM-811 vs. Li^+/Li of cell 2 for the 19th cycle (black curves, after the first LDE XPD data point, BOT) and for the 973rd cycle (blue curves, close to the last LDE XPD data point in the 975th cycle, EOT). It can be seen that the overpotential of the cathode (solid lines) increases drastically with cycling, as already indicated by its mean voltage evolution. Because cycling was carried out between fixed cathode voltage limits (3.0 and 4.5 V vs. Li^+/Li), this increase of overpotential contributes significantly to the observed capacity fading, as the accessible capacity window gets narrowed from both sides.^{19,58} On the other hand, the voltage profile of the graphite anode (dashed lines) shows no significant change with cycling.

In the literature, various factors are discussed which might cause the capacity fading for Ni-rich NCMs in the absence of a loss of cyclable lithium (i.e., in half-cells with lithium anodes or, as in this study, in full-cells with pre-lithiated graphite anodes), as seen in Figure 2. Amongst others, bulk structural changes such as cation disorder are identified as possible reason.⁵² A notably increased fraction of Ni in the Li layer would not only reduce the number of active Li sites, but also gives rise to an increased polarization.⁵⁹ Contact loss in the CAM due to pronounced particle cracking¹³ and surface instabilities,²⁰ however, are also reported to lead to a capacity loss due to impedance build-up. At the same time, both cracking and surface instabilities might cause a capacity loss due to material loss in the form of isolated particles or reconstructed phases, which are electrochemically inactive. In the following, the reasons for the continuous capacity fading observed in Figure 2 are analyzed by a combination of various techniques, with emphasis on the long-duration experiment XPD data.

XPD analysis with respect to bulk stability and cation mixing.— Starting our XPD analysis, we first examined whether any reversible phase transformations could be observed. For instance, for LiNiO_2 , there are literature reports on the reversible phase transformation from a hexagonal to a monoclinic structure (H1-M transformation) and further on to new hexagonal versions (M-H2 and H2-H3 transformations) upon delithiation.⁷ The H1-M transformation is accompanied by the splitting of the original (101), (012), and (104) reflections in the hexagonal symmetry, whereas the H2-H3 transformation involves an abrupt contraction of the lattice parameter c . In our study, no peak splitting

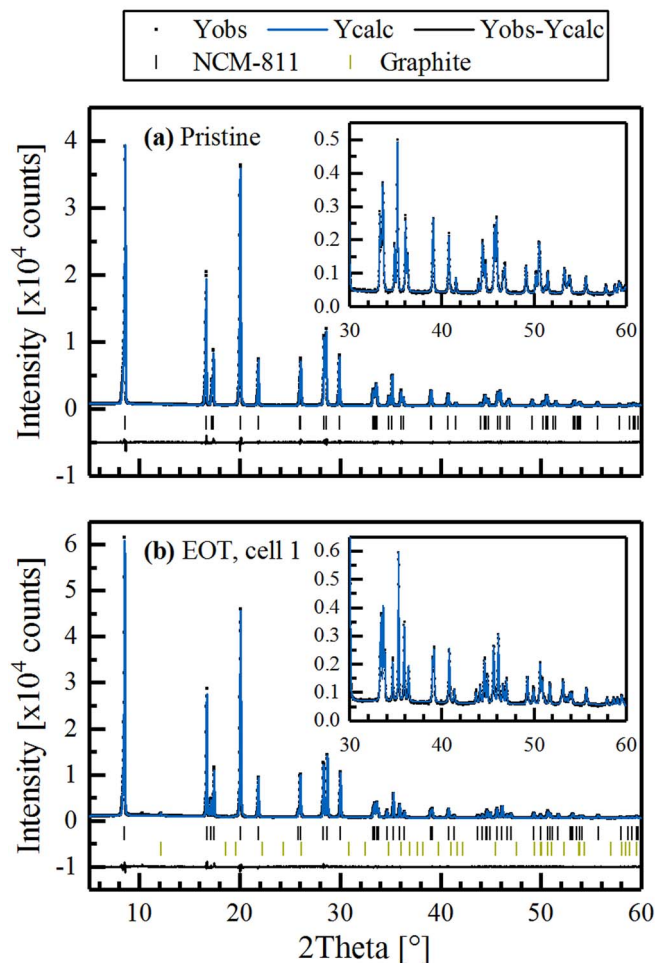


Figure 3. Refinement of ex situ L-XPD data based on capillary measurements of (a) pristine and (b) harvested EOT NCM-811 powder (from cell 1) in the common $R\bar{3}m$ space group. The data were collected at the in-house Mo-diffractometer ($\lambda = 0.7093 \text{ \AA}$). The observed (black points), calculated (blue lines), and difference diffraction profiles (black lines) are shown together with the position of the Bragg peaks of NCM-811 (black ticks) and graphite (green ticks). The insets show a magnification of the high-angular range. Note that the EOT NCM-811 electrode sample contains 2 wt% conductive graphite, which was included into the refinement (strongest reflection at $\approx 12^\circ$). The refinement results are summarized in Table I.

and only a gradual contraction of the c parameter were observed. In the study of Ryu et al.,⁶⁰ these LiNiO_2 -like transformations were only seen for NCM materials with a Ni content of 90% or higher. Other authors report on an irreversible thermal reconstruction of the rhombohedral to a spinel structure of $\text{Li}_{0.5}\text{NiO}_2$, indicated by a coalescence of the (018) and (110) reflections,⁶¹ which we could not observe here by electrochemical cycling.

Next, we examined the XPD patterns for any sign of cation disorder between the Li and transition-metal layer, i.e., for Li-Ni mixing. The refinement of this sensitive parameter has proved to be difficult, especially in the case of in situ XPD data due to the overlapping reflections from other cell components (Al and Cu) and the complex background patterns (see paragraphs S1 and S2 in the SI). Furthermore, we observed a significant correlation between the Li occupancy and cation disorder, as it is also known from the literature.³⁴ The refinement of the cation disorder was therefore conducted with ex situ L-XPD data from capillary measurements with pristine NCM-811 powder and discharged NCM-811 cathodes harvested at EOT. These data are shown in Figure 3, and the refinement results are summarized in Table I, whereby the remaining Li content, x_{Li} , of the EOT samples was determined from the c/a calibration curves discussed in the following

Table I. Refinement results of pristine NCM-811 and NCM-811 electrodes harvested at EOT, based on ex situ L-XPD capillary measurements at a Mo-diffractometer and refined in the common $R\bar{3}m$ space group. The diffractograms for pristine NCM-811 and the electrode harvested at EOT from cell 1 are shown in Figure 3. The table summarizes quality factors (R -values), lattice parameters and the thereof determined Li content and atomic site-specific information (including Li-Ni mixing, fractional z -coordinate of O, and thermal displacement parameters). The b values were constrained to be the same for all elements on one site. Errors given in parenthesis.

	Pristine	EOT, cell 1	EOT, cell 2
R_{wp} [%]	4.52	4.48	4.84
R_{bragg} [%]	1.14	1.04	1.49
χ^2	1.99	2.63	2.04
a [\AA]	2.87212(2)	2.85945(2)	2.85931(3)
c [\AA]	14.2058(2)	14.2902(2)	14.2820(3)
c/a [-]	4.94609(7)	4.99756(7)	4.9949(1)
x_{Li} [-]	1.01 ^a	0.79 ^b	0.80 ^b
Li-Ni mixing [%] ^c	3.1(1)	2.0(1)	3.1(1)
$z_{6c,O}$ [-]	0.24156(7)	0.23908(8)	0.2396(1)
$b_{3a,\text{Li}}$ [\AA^2]	1.22(9)	0.7(1)	1.1(2)
$b_{3b,\text{TM}}$ [\AA^2]	0.171(8)	0.298(9)	0.08(1)
$b_{6c,O}$ [\AA^2]	0.62(2)	0.82(3)	0.47(3)

^aThe Li content of the pristine material was fixed to the elemental analysis results ($\text{Li}_{1.01}\text{Ni}_{0.79}\text{Co}_{0.10}\text{Mn}_{0.10}\text{O}_2$).

^bThe Li content of the EOT materials was calculated from the low-SOC c/a calibration curve, as shown in Figure 5a and in paragraph S1 in the SI.

^cLi-Ni mixing gives the percentage of Ni on the 3a site of the Li layer relative to the total available occupancy of the 3a site.

section (see Figure 5a). These refinements give a Li-Ni mixing of 3.1(1)% for the pristine and EOT sample of cell 2. The EOT sample of cell 1 gives a reproducible cation disorder of 2.0(1)%.

For the refinement of the in situ S-XPD data, the cation disorder was therefore fixed to the value obtained from the ex situ L-XPD capillary data, because there the parameter could be determined reliably and without any overlapping reflections. In the Rietveld refinement, the very sensitive cation disorder parameter correlates strongest to the thermal displacement parameter $b_{3a,\text{Li}}$ ($\approx 75\%$) and the scale factor ($\approx 65\%$). However, all b values are in a reasonable range.^{34,39} Fixing the EOT b values to the pristine b values increases the Li-Ni disorder only by $\approx 0.2\%$. Thus, we can conclude with confidence that the Li-Ni mixing is barely affected by 1000 charge/discharge cycles and does not contribute to the observed capacity loss. Since the peak broadening of the samples is also very similar (see Table S2 in the SI for the in situ S-XPD data), all these results prove that there are no remarkable bulk structural changes observed in the NCM-811 CAM upon long-term cycling with an upper cut-off voltage of 4.5 V vs. Li^+/Li . This is in agreement with a study over 300 cycles for NCM-811/graphite full-cells including XPD data performed by Kim et al.,⁶² even though it should be noted that the upper cut-off voltage in their study was only 4.2 V. Furthermore, there are literature reports (without specifically refining Li-Ni mixing) on the bulk stability of Ni-rich CAMs like $\text{LiNi}_{0.76}\text{Co}_{0.14}\text{Al}_{0.10}\text{O}_2$, which was cycled over 1000 cycles also to 4.2 V,⁶³ and NCM-523 cycled 50 times to a cut-off potential as high as 4.8 V vs. Li^+/Li .⁵⁸ This is in contrast to a study of Li et al.,¹¹ claiming the structural instability of Ni-rich CAMs, $\text{LiNi}_{0.80}\text{Co}_{0.15}\text{Al}_{0.05}\text{O}_2$ and $\text{LiNi}_{0.70}\text{Co}_{0.15}\text{Mn}_{0.15}\text{O}_2$, which showed an increase of Li-Ni disorder from 2–3% to 9–13% after cycling over 1500 charge/discharge cycles between 3.0 V and a relatively high upper cut-off voltage of 4.4 V. In our case, it can be concluded that the NCM-811 bulk structure is stable over 1000 cycles, even if a cut-off potential as high as 4.5 V vs. Li^+/Li is chosen.

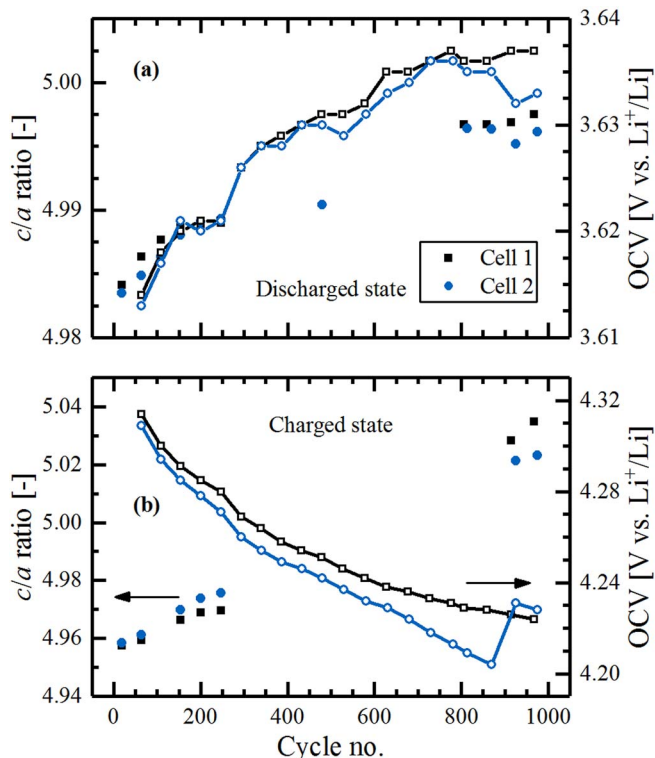


Figure 4. Evolution of the c/a ratio (filled symbols, left y-axes) and the OCV (line and empty symbols, right y-axes) in the (a) discharged and (b) charged state of NCM-811, determined from the in situ S-XPD data obtained from the two cells cycled at the Diamond Light Source. Missing c/a data points are due to a long beam shut-down.

Lattice parameter evolution monitored via XPD analysis.—From the refinement of the in situ S-XPD patterns, the lattice parameters of NCM-811 were obtained in charged and discharged state over the course of almost 1000 cycles for the two cells (more refinement results shown in paragraph S2 in the SI). The lattice parameter ratio c/a is shown in Figure 4 (filled symbols, left y-axes) together with the OCV at which the respective data were measured (empty symbols, right y-axes). According to literature data, the c/a ratio is the most reliable measure of lattice expansion (in c -direction) and compression (in a, b direction) induced by Li extraction and insertion in NCM materials.⁶⁴ It can be seen that in both charged and discharged state the c/a ratio increases during the experiment (see filled symbols). Furthermore, the OCV was found to change over the course of extended cycling, increasing in the discharged state (empty symbols in Figure 4a) and decreasing in the charged state (empty symbols in Figure 4b). For a stable bulk material – which we can assume based on the ex situ L-XPD data discussed above – it is known that the OCV scales with the SOC of the material, i.e., the higher the SOC, the higher the respective OCV value. Thus, from the OCV evolution shown in Figure 4, we can conclude that the effective SOC window becomes smaller over the course of cycling. This is in agreement with the observed capacity loss and overpotential increase of the NCM-811 electrode (see Figure 2). Here, we should note that the jump in the OCV (≈ 30 mV) observed for cell 2 after ≈ 900 cycles is related to the change in cell contacting resistance at this point and also reflected in an increase in cell capacity (see Figure 2a), as discussed above.

To understand whether this is consistent with the observed increase of the c/a ratio over cycling in both the charged and discharged state (filled symbols in Figures 4a, 4b), one has to consider the relationship between the c/a ratio and the lithium content, x_{Li} , or the SOC of NCM materials: the c/a ratio initially increases upon charging until it reaches a maximum at $\approx 60\%$ SOC (i.e., $x_{Li} \approx 0.4$) and then decreases upon

further increasing the SOC.^{51,60,64,65} Thus, the observed increase in the c/a parameter in the discharged state (SOC $\ll 60\%$) and in the charged state (SOC always $>60\%$), clearly indicates a shrinkage in the capacity window, which at least qualitatively is consistent with the OCV evolution.

To convert the qualitative OCV and c/a analysis into a quantification of capacity losses in the charged and discharged state, the c/a curve for the first two/three cycles was measured to serve as a calibration curve of the c/a ratio vs. capacity (more precisely x_{Li}) or OCV, as will be described in the following. The detailed approach and the respective data sets from in situ XPD (i.e., complete XPD pattern collected at OCV conditions at different SOC steps over 2 cycles) and operando XPD (i.e., continuous data collection of (003) and (110) reflection during 3 cycles) are described in the Experimental section and are discussed in detail in paragraph S3 in the SI. The thus obtained relationship between the c/a ratio and the lithium content x_{Li} of NCM-811 is shown exemplarily for the 2nd discharge cycle in Figure 5a (measured in operando mode), which is in agreement with literature reports.^{60,65,66}

Next, the lattice parameters obtained from the in situ S-XPD data during long-term cycling were used to compute the changes of the c/a ratio, from which the Li content x_{Li} in the cycled NCM-811 (i.e., in $\text{Li}_x\text{Ni}_{0.79}\text{Co}_{0.10}\text{Mn}_{0.10}\text{O}_2$) could be determined, as was done by Buchberger et al.⁵¹ The relationship between the c/a ratio and x_{Li} is given in Figure 5a and in paragraph S1 in the SI. Here, the advantages of using the c/a ratio instead of only the lattice parameters becomes evident: (i) the c/a ratio is close to linearity in the x_{Li} ranges of interest; and, (ii) small misalignments of the cells in the geometry of the diffractometer would not falsify the result, because the error gets cancelled out by taking the ratio of both lattice parameters. From the S-XPD analysis shown in Figure 4, we know that the c/a ratio in both the discharged state (low SOC) and the charged state (high SOC) increases with cycling. The grey bars in Figure 5a mark the c/a ratio changes over 1000 cycles in both the discharged state (left bar) and the charged state (right bar), based on the data in Figure 4 (filled symbols). With the obtained operando L-XPD calibration curve (black symbols and interpolating line in Figure 5a), a mathematical relationship between x_{Li} and c/a can now be established. At low SOC ($0.62 \leq x_{Li} \leq 0.91$), i.e., in the discharged state, this is best described by a quadratic equation of c/a as function of x_{Li} (highlighted in blue in Figure 5a, with the equation given in the figure, and also as x_{Li} as a function of c/a in equation (S1) in the SI). At high SOC ($0.12 \leq x_{Li} \leq 0.23$), i.e., in the charged state, there is a linear dependence between c/a and x_{Li} (highlighted in green, with the equation given in the figure and as equation (S2) in the SI).

With the values for c/a in the discharged and charged state over 1000 cycles (from Figure 4), the capacity losses at low and high SOC in the i^{th} cycle ($\Delta C_{\text{Discharge}}^{\text{BOT} \rightarrow i}$ and $\Delta C_{\text{Charge}}^{\text{BOT} \rightarrow i}$) relative to the first in situ S-XPD data point in the 18th cycle (BOT) can now be quantified and then compared to the electrochemical capacity loss ($\Delta C_{\text{EC}}^{\text{BOT} \rightarrow i}$). The applied calculations are explained in the following, whereby a “ Δ ” represents a difference between two specific states. Firstly, the electrochemical capacity loss between the i^{th} cycle and at BOT (18th cycle), $\Delta C_{\text{EC}}^{\text{BOT} \rightarrow i}$, is defined by the difference of the discharge capacity in the i^{th} cycle, C_{EC}^i , and that at BOT, $C_{\text{EC}}^{\text{BOT}}$:

$$\Delta C_{\text{EC}}^{\text{BOT} \rightarrow i} = C_{\text{EC}}^{\text{BOT}} - C_{\text{EC}}^i \quad [1]$$

This can be compared to the capacity loss inferred from the in situ S-XPD data, namely to the sum of the calculated capacity losses referenced to BOT in the discharged state, $\Delta C_{\text{Discharge}}^{\text{BOT} \rightarrow i}$, and in the charged state, $\Delta C_{\text{Charge}}^{\text{BOT} \rightarrow i}$:

$$\Delta C_{\text{Overpotential}}^{\text{BOT} \rightarrow i} = \Delta C_{\text{Discharge}}^{\text{BOT} \rightarrow i} + \Delta C_{\text{Charge}}^{\text{BOT} \rightarrow i} \quad [2]$$

Both of these XPD-deduced capacity loss values can be calculated for the i^{th} cycle relative to BOT by taking the difference between the respective x_{Li} values between the i^{th} cycle and BOT (Δx_{Li}) in either the discharged state ($x_{\text{Li,dis}}^i - x_{\text{Li,dis}}^{\text{BOT}}$) or the charged state ($x_{\text{Li,cha}}^{\text{BOT}} - x_{\text{Li,cha}}^i$), which are obtained by the measured c/a ratios using the mathematical

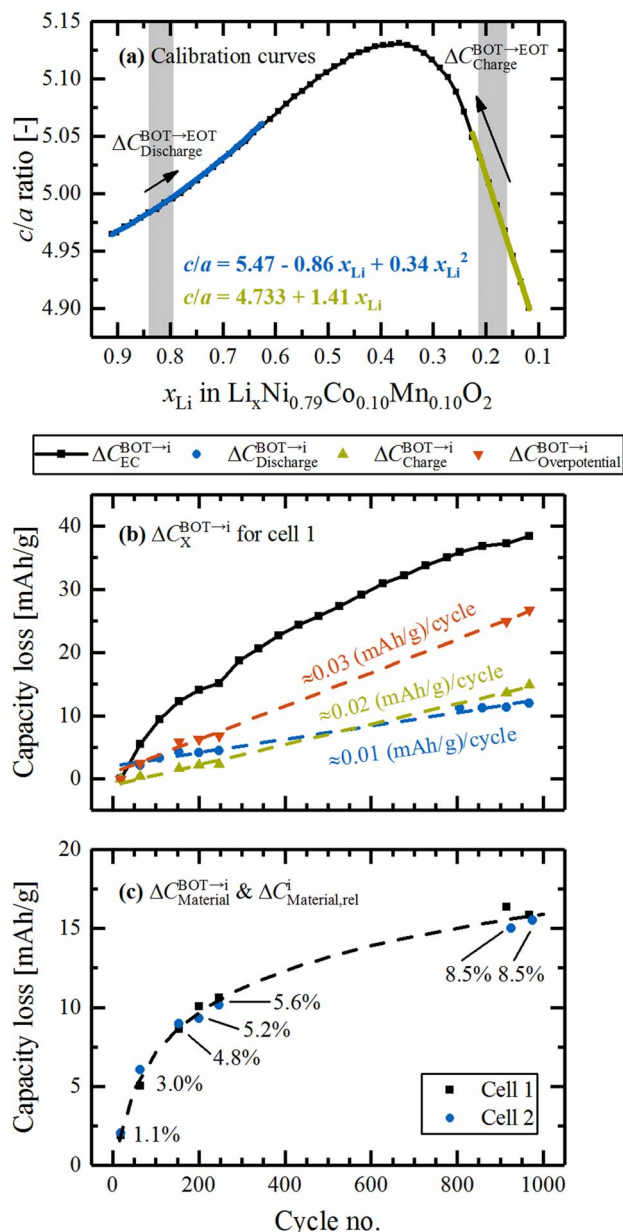


Figure 5. (a) Dependence of the c/a ratio on the Li content x_{Li} for the pristine NCM-811 CAM determined by operando L-XPD (black symbols and interpolating line, shown exemplarily for the 2nd discharge cycle). The quadratic and linear fits at low and high SOC are shown in blue and green, respectively (average from the first three discharge cycles, equations given in the plot and in paragraph S1 of the SI). Furthermore, the evolution of the c/a ratio from BOT to EOT during the long-term cycling study is indicated by the grey bars and arrows (based on the filled symbols in Figure 4). (b) Capacity loss relative to BOT calculated from electrochemical data ($\Delta C_{EC}^{BOT \rightarrow i}$, Eq. 1) and from changes of x_{Li} obtained by in situ S-XPD in the discharged ($\Delta C_{Discharge}^{BOT \rightarrow i}$, Eq. 3) and charged state ($\Delta C_{Charge}^{BOT \rightarrow i}$, Eq. 4) as well as the sum of both ($\Delta C_{Overpotential}^{BOT \rightarrow i}$, Eq. 2). (c) Capacity loss attributed to a material loss depicted in absolute values ($\Delta C_{Material}^{BOT \rightarrow i}$, Eq. 6, individual data points for cell 1 and 2) and relative to the pristine CAM ($\Delta C_{Material,rel}^i$, Eq. 7, percentages given for each cycle as mean value from cell 1 and 2).

relationships between the c/a ratio and x_{Li} (see equations (S1) and (S2) in paragraph S1 of the SI). To convert this Δx_{Li} difference into a specific capacity, the second term on the right-hand side of Equations 3 and 4 serves as a conversion factor relating 1.01 mol Li to the theoretical capacity of 274 mAh/g for complete Li extraction in the

here used NCM-811 material ($Li_{1.01}Ni_{0.79}Co_{0.10}Mn_{0.10}O_2$, theoretical capacity includes surface impurities, see Experimental section).

$$\Delta C_{Discharge}^{BOT \rightarrow i} = (x_{Li,dis}^i - x_{Li,dis}^{BOT}) \cdot \frac{274 \text{ mAh/g}}{1.01} \quad [3]$$

$$\Delta C_{Charge}^{BOT \rightarrow i} = (x_{Li,cha}^{BOT} - x_{Li,cha}^i) \cdot \frac{274 \text{ mAh/g}}{1.01} \quad [4]$$

In this case, $\Delta C_{Overpotential}^{BOT \rightarrow i}$ (Equation 2) accounts for the accumulated capacity loss between BOT and the i^{th} cycle due to an increasing overpotential, as deduced from the in situ S-XPD data. If the capacity loss over cycling were only due to an increasing NCM-811 overpotential, $\Delta C_{Overpotential}^{BOT \rightarrow i}$ would have to be identical with the electrochemically determined capacity loss $\Delta C_{EC}^{BOT \rightarrow i}$ (see Equation 1). On the other hand, if part of the NCM-811 would either become electrochemically inactive by a loss of material (e.g., by dissolution) or by the formation of an inactive phase, $\Delta C_{EC}^{BOT \rightarrow i}$ would be larger than $\Delta C_{Overpotential}^{BOT \rightarrow i}$.

The application of these calculations is shown for cell 1 in Figure 5b, where we compare the electrochemically measured capacity losses, $\Delta C_{EC}^{BOT \rightarrow i}$ (black symbols), with those calculated based on the lattice parameter changes, namely the sum of $\Delta C_{Discharge}^{BOT \rightarrow i}$ (blue symbols) and $\Delta C_{Charge}^{BOT \rightarrow i}$ (green symbols), equating to $\Delta C_{Overpotential}^{BOT \rightarrow i}$ (red symbols). The capacity loss $\Delta C_{Overpotential}^{BOT \rightarrow i}$ is caused by the increased overpotential of the NCM-811 CAM (see Figure 2c), which results in a smaller effective SOC window because the upper and lower cut-off potentials are reached earlier, corresponding to a smaller cyclable Δx_{Li} . In the lithiated state, the capacity loss calculated via $\Delta(c/a)$ is ≈ 0.01 (mAh/g)/cycle ($\Delta C_{Discharge}^{BOT \rightarrow i}$, blue curve in Figure 5b), while it is roughly doubled in the delithiated state ($\Delta C_{Charge}^{BOT \rightarrow i}$, green curve in Figure 5b). This corresponds to a shrinkage of the SOC window from initially $0.16 \leq x_{Li} \leq 0.84$ ($\Delta x_{Li} = 0.68$) for cell 1 in cycle 18 to $0.21 \leq x_{Li} \leq 0.79$ ($\Delta x_{Li} = 0.58$) after 1000 cycles. This shrinkage of the exchanged amount of lithium per cycle determined by in situ S-XPD translates into a capacity loss between BOT and EOT of $\Delta C_{Overpotential}^{BOT \rightarrow i} = 26.8$ mAh/g (\equiv value of the red curve at EOT in Figure 5b), which is substantially smaller than the electrochemically measured capacity loss from BOT to EOT of $\Delta C_{EC}^{BOT \rightarrow i} = 38.4$ mAh/g (\equiv value of the black curve at EOT in Figure 5b). The discrepancy between $\Delta C_{Overpotential}^{BOT \rightarrow i}$ and $\Delta C_{EC}^{BOT \rightarrow i}$ must be caused by a loss of active NCM-811, meaning that a portion of the material has either disappeared or is no longer participating in the electrochemical processes. As described in the literature, the capacity loss could be caused by the formation of an oxygen-deficient and electrochemically inactive phase formed at the surface of the NCM-811 particles, which transforms gradually into an insulating spinel/rock-salt-type layer and thereby also causes an impedance growth of the CAM.^{18,19,67,68} Another possible scenario is the formation of electronically isolated particles caused by cracking phenomena, which would then become electrochemically inactive.¹³ As we observe no second NCM-811 phase with shifted reflections (i.e., constant lattice parameters) in the patterns in neither discharged nor charged state, the formation of electronically isolated particles can be ruled out. Moreover, *post mortem* elemental analysis revealed only a minor amount of TMs deposited on the graphite anode at EOT (corresponding to ≈ 0.22 mol%_{TM} when referenced to the original NCM-811 material, which would amount to a maximum capacity loss of ≈ 2.4 mAh/g as described in paragraph S3 of the SI), indicating that CAM dissolution is a rather negligible contribution to the overall capacity loss after ≈ 1000 cycles of the NCM-811 CAM between 3.0 and 4.5 V vs. Li^+/Li . This further supports the hypothesis that the loss of active material may be due to the formation of an electrochemically inactive surface layer.

To more precisely quantify the loss of electrochemically active material over cycling, one can compare the absolute electrochemically observed capacity in the i^{th} cycle, C_{EC}^i , to the effective capacity window in the i^{th} cycle expected from the Δx_{Li} range (i.e., $x_{Li,cha}^i - x_{Li,dis}^i$), as determined from the in situ S-XPD analysis and converted into a

capacity, C_{XPD}^i :

$$C_{\text{XPD}}^i = (x_{\text{Li,cha}}^i - x_{\text{Li,dis}}^i) \cdot \frac{274 \text{ mAh/g}}{1.01} = \Delta x_{\text{Li}}^i \cdot \frac{274 \text{ mAh/g}}{1.01} \quad [5]$$

If 100% of the original NCM-811 material were active, the electrochemical capacity in the i^{th} cycle, C_{EC}^i , and the capacity predicted by the Δx_{Li} range, C_{XPD}^i , would have to be equal. If, however, a part of the CAM becomes electrochemically inactive, the capacity expected from the XPD data, C_{XPD}^i , would be larger than what can be observed, C_{EC}^i , because the Δx_{Li} range determined from XPD is applied for the whole CAM (i.e., the CAM fraction from XPD analysis appears always as 100%). Therefore, a loss of electrochemically active material by the i^{th} cycle, $\Delta C_{\text{Material}}^i$, would correspond to the difference between C_{XPD}^i (capacity if no cyclable material would have been lost) and the actual electrochemical capacity in the i^{th} cycle:

$$\Delta C_{\text{Material}}^{\text{BOT} \rightarrow i} = (C_{\text{XPD}}^i - C_{\text{EC}}^i) \cdot \frac{\Delta x_{\text{Li}}^{\text{BOT}}}{\Delta x_{\text{Li}}^i} \quad [6]$$

The correction factor of $\Delta x_{\text{Li}}^{\text{BOT}}/\Delta x_{\text{Li}}^i$ takes into account that the material loss goes typically hand in hand with an increased overpotential (i.e., $\Delta x_{\text{Li}}^{\text{BOT}} > \Delta x_{\text{Li}}^i$). Consequently, the material loss relative to BOT has to be referred to the broader $\Delta x_{\text{Li}}^{\text{BOT}}$ range and BOT should ideally be a state where no material loss has yet occurred (i.e., one of the very first cycles). More intuitively, the material loss can also be expressed in percentage terms as the electrochemically inactive phase fraction relative to the pristine CAM:

$$\Delta C_{\text{Material,rel}}^i = \frac{C_{\text{XPD}}^i - C_{\text{EC}}^i}{C_{\text{XPD}}^i} \quad [7]$$

Here, no correction is necessary since the equation only involves data from the i^{th} cycle, with C_{XPD}^i being the maximum capacity, which can be achieved with the actually present overpotential of the aged CAM in the i^{th} cycle.

The thus calculated capacity loss due to the loss of electrochemically active material, $\Delta C_{\text{Material}}^{\text{BOT} \rightarrow i}$, for both cell 1 and cell 2 as well as the average share of lost material relative to the pristine CAM, $\Delta C_{\text{Material,rel}}^i$, are shown in Figure 5c. The curve of the material loss shows a steep increase during the first 300 cycles and levels out afterwards, suggesting that most material losses happen in the first 300 cycles. It is known for regular NCMs^{15,18} as well as for Li-rich NCMs^{17,69} that a surface reconstruction is triggered by the loss of oxygen, which happens mainly in the very first cycles, especially if the cathode is charged over 80% SOC. Here, an SOC of $\approx 85\%$ is reached during the first two C/10 formation cycles. On the other hand, HR-TEM images have shown that the actual reconstruction happens within 20–50 cycles for Li-rich NCMs at 25°C.¹⁷ As vacancies in the transition-metal layer probably facilitate the reconstruction in Li-rich NCMs, it is reasonable to assume that this process takes longer for regular NCMs (here 200–300 cycles). At the end-of-test, the material loss for both cells adds up to $\approx 15.8 \text{ mAh/g}$ or 8.5% (average of the data for both cells at ≈ 1000 cycles in Figure 5c). As we propose that this materials loss is due to the formation of a thin surface layer in the nm range with a possibly amorphous character, it is not unexpected that it is not visible as additional phase in the diffractograms, similar to the finding for aged NCMs in the literature.^{18,51} For this reason, we also tried to quantify the electrochemically active NCM-811 fraction over the course of the cycling study by normalizing its scale factor (measure of the intensity of this phase) to the intensity of stable “internal standards” in the cell (see Figure S4 in the SI). For this analysis, we used the polymer peaks from the pouch foil as well as the intensity of the (111) reflection of Al and Cu, which were both refined with a structure-independent Pawley fit. As can be seen in Figure S4, the results have a relatively large scatter, but a loss of a fraction of the active NCM-811 phase from BOT to EOT can be concluded as general trend.

The above analysis has shown that we can differentiate two main contributions to the capacity loss of NCM-811, namely the overpotential-induced loss and the actual loss of cyclable material. As only the electrochemically active material can undergo a capacity

loss due to an increasing overpotential, $\Delta C_{\text{Overpotential}}^{\text{BOT} \rightarrow i}$ has to be corrected by the NMC-811 phase fraction which has been lost up to the respective cycle:

$$\Delta C_{\text{Overpotential,corr}}^{\text{BOT} \rightarrow i} = \Delta C_{\text{Overpotential}}^{\text{BOT} \rightarrow i} \cdot (1 - \Delta C_{\text{Material,rel}}^i) \quad [8]$$

The same correction applies to the individual contributions in the discharged ($\Delta C_{\text{Discharge}}^{\text{BOT} \rightarrow i}$) and charged state ($\Delta C_{\text{Charge}}^{\text{BOT} \rightarrow i}$, see Equation 2). Since the material loss amounts to 8.5% at the end-of-test, $\Delta C_{\text{Overpotential}}^{\text{BOT} \rightarrow \text{EOT}} = 26.8 \text{ mAh/g}$ for cell 1 in Figure 5b reduces to 24.5 mAh/g after correction. Thus, the sum of both loss terms from BOT to EOT, $\Delta C_{\text{Overpotential,corr}}^{\text{BOT} \rightarrow \text{EOT}}$ and $\Delta C_{\text{Material}}^{\text{BOT} \rightarrow \text{EOT}}$ (15.8 mAh/g), amounts to 40.3 mAh/g for cell 1. This calculated value is slightly higher than the actual capacity loss of $\Delta C_{\text{EC}}^{\text{BOT} \rightarrow \text{EOT}} = 38.4 \text{ mAh/g}$ due to the material loss which was already acquired until the begin-of-test (1.9 mAh/g in the 18th cycle, see Figure 5c).

Bulk stability vs. surface instability.—In the following, XPD data from which we have inferred the stability of the bulk of NCM-811 (Figure 6a) are contrasted with impedance data from which we will get insights into the long-term stability of the NCM-811 surface (Figure 6b). Let us first focus on Figure 6a, where the c/a ratio is shown as a function of the open circuit voltage for the in situ L-XPD data (i) from the first two cycles of the NCM-811 cathode (black symbols/lines) and (ii) from the harvested EOT cathode of cell 1 (blue symbols/lines)

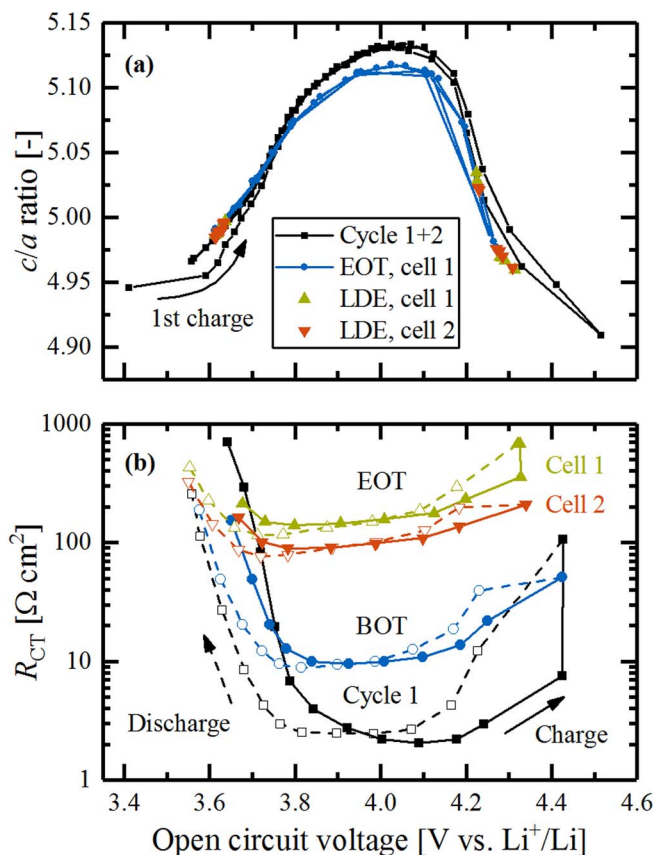


Figure 6. (a) Comparison of the in situ L-XPD c/a curves of a fresh NCM-811 cathode in cycle 1 and 2 (black symbols/lines) and for the EOT cathode (harvested from cell 1, blue symbols/lines) cycled vs. a lithium anode with the c/a data points collected during the long-term S-XPD study from cells 1 and 2 (green and red symbols, labeled as LDE, same data as in Figure 4). (b) Comparison of the charge-transfer resistance of NCM-811 cathodes in the first cycle, at BOT, and at EOT for both long-term cycled cells, measured with a GWRE in a NCM-811/pre-lithiated graphite setup at 25°C. The electrodes in cycle 1 and BOT are a different set than that at EOT. Both the c/a data in panel (a) and the R_{CT} data in panel (b) are shown as a function of the OCV value, at which the data points were measured.

as well as for the in situ S-XPD data from both cells over the course of cycling (green and red symbols, labeled as LDE cells). Note that the OCV values versus the Li-CE (for the L-XPD data) or the Li-RE (for the S-XPD data cycled vs. a pre-lithiated graphite CE) are exactly known from each in situ measurement, i.e., the datasets can be directly compared with each other without any correction. The Rietveld refinement of the capillary data (Figure 3) already indicated the bulk stability over the course of the 1000 cycles. The LDE S-XPD *ca* data (green and red points in Figure 6a, which are the same data as in Figure 4) agree fairly well with the in situ L-XPD calibration curves of the first two cycles (black points/lines) and the EOT sample (blue points/lines). This proves that the *ca* calibration curve taken for NCM-811 in the first few cycles and used to quantify the lithium content x_{Li} at low or high SOC, is also valid for NCM-811 aged over the course of 1000 cycles, so that the XPD analysis conducted in Figure 5 is feasible. The small deviation of the first *ca* points in the first charge from the first discharge and the subsequent cycle is discussed in paragraph S3 in the SI and shown in more detail in Figure S6. Furthermore, the discrepancy of the EOT curve in the mid-voltage region is probably caused by a minor amount of dissolved transition-metals (≈ 0.22 mol% TMs detected by ICP-OES on the graphite anode at EOT). The observed discrepancy is also discussed in context with Figure S6 in paragraph S3 of the SI.

As described above, a growing overpotential on the cathode was identified to be a major reason for the observed capacity loss in NCM-811/graphite full-cells based on the XPD analysis, as shown by $\Delta C_{\text{Overpotential}}^{\text{BOT} \rightarrow \text{EOT}}$ in Figure 5b. It has been reported in the literature that the formation of a spinel or rock-salt-like structure at the surface of NCM cathode materials leads to a drastic increase in the charge-transfer resistance.^{15,18,19} To further analyze the overpotential build-up deduced from our XPD analysis (Figure 5) and the charge/discharge curve profiles (Figure 2a and Figure S9), we determined the cathode impedance of NCM-811 cathodes after a different number of cycles, using a three-electrode setup with a micro-reference electrode. Figure S7 in the SI shows exemplary cathode impedance spectra taken at ≈ 4.0 V during charge of NCM-811 cathodes in the first cycle, in the 18th cycle (corresponding to BOT), and after 1000 cycles (EOT) from a harvested NCM-811 cathode. The spectra exhibit a semicircle at low frequencies, which could be assigned to the charge-transfer resistance, R_{CT} , as described in paragraph S4 in the SI. As the value of R_{CT} is SOC-dependent, these impedance measurements were conducted during OCV at different points during charge and discharge, namely at steps of 20 mAh/g, in a similar fashion as the in situ XPD measurements in Figure 6a. The resulting R_{CT} values are plotted versus OCV in Figure 6b. As was already mentioned above, there is no need to correct for any shift in capacity (x-axis) when plotting vs. OCV, because this is already a measure of the bulk state-of-charge or the lithium content. All R_{CT} curves depicted in Figure 6b have a characteristic minimum around ≈ 4.0 V and increasing values toward the SOC limits, analogous to what has been reported for HE-NCM.⁷⁰ A comparison of the curves during charge at ≈ 4.0 V is consistent with the observed increase of the NCM-811 cathode overpotential, with the charge-transfer resistance found to increase from $\approx 2 \Omega \text{ cm}^2$ to $\approx 10 \Omega \text{ cm}^2$ over the first 18 cycles (black vs. blue curve) and further up to $\approx 100\text{--}150 \Omega \text{ cm}^2$ after 1000 cycles (green and red curve for EOT cell 1 and 2). This means that the impedance growth for cell 2 amounts to $\approx 90 \Omega \text{ cm}^2$ from BOT to EOT, which at a rate of $C/2$ ($\equiv 0.75 \text{ mA/cm}^2$) would equate to an additional overpotential of $\approx 70 \text{ mV}$ (a slightly higher impedance growth of $140 \Omega \text{ cm}^2$ and a higher projected overpotential of $\approx 105 \text{ mV}$ is obtained for cell 1). The overpotential growth calculated from the R_{CT} increase for cell 2 is reasonably consistent with what we observed from the cathode half-cell voltage profiles of cell 2 shown in Figure 2c. There, the difference between charge and discharge voltage at mid-SOC (near 4 V) increases by $\approx 240 \text{ mV}$ between cycle 19 and cycle 973, compared to the R_{CT} -based prediction of $\approx 140 \text{ mV}$. A more detailed description of this overpotential build-up plotted over the whole SOC window is depicted in Figure S9 of the SI. In addition, there is also a difference plot between the cathode half-cell voltage profiles at EOT and cycle 250 versus BOT, indicating that the

overpotential increase can be seen over the whole SOC window and that it is more pronounced during the discharge than during charge, an observation which for yet unknown reasons is at variance with the R_{CT} data in Figure 6b. Overall, however, the cathode potential vs. capacity curves can be used as an indicator for the impedance build-up, as they correlate reasonably well with cathode impedance based R_{CT} values. This fact is further utilized to analyze the evolution of the overpotential build-up over cycling.

While the impedance growth over the 1000 cycles shown in Figure 6b can account for a significant part of the NCM-811 capacity loss, our XPD analysis shown in Figure 5 also indicates that there must be an additional loss of cyclable material, which was found to be most pronounced during the first 300 cycles (see Figure 5c). In this context, it has been suggested that oxygen release takes place in surface-near regions of NCMs or HE-NCMs, leading to a highly disordered oxygen-deficient surface layer which during subsequent cycling transforms into a resistive spinel/rock-salt-like layer, accompanied by an impedance build-up.^{15–19,71} If material at the NCM-811 particle surface were to transform directly into a resistive layer, the impedance build-up should follow the same trend over cycling as the material loss derived from the $\Delta C_{\text{Material}}^i$ data, namely increasing rapidly until cycle 300, followed by a more gradual increase afterwards (see Figure 5c). However, the evolution of the overpotential on the cathode half-cell voltage profile does not follow the trend of the material loss (see comparison of cycle 250 with BOT in Figure S9 in the SI). Indeed, the voltage profile in cycle 250 does not exhibit a significant overpotential ($\approx 40 \text{ mV}$ for cell 2 near 4.0 V during charge, highlighted by a grey bar in Figure S9 in the SI), although at the same cycle number, $\Delta C_{\text{Material}}^i$ shown in Figure 5c already indicates a substantial loss of cyclable material. Thus, we could further confirm the observations made in the literature^{18,19} on the early transformation of the surface-near region of NCM, then followed by a subsequent, more gradual transformation into a resistive surface layer. Summarizing our findings so far: R_{CT} is the origin of the growing cathode overpotential developing gradually over the course of cycling. This, in turn, causes the cell to run earlier into its voltage limits, thereby shrinking the effective capacity window (Δx_{Li}). We showed that this capacity loss due to an increased overpotential can be monitored by XPD, as shown in Figure 5 and Figure 6a. Thus, the surface instability of the NCM-811 cathode active material is the dominant factor contributing to capacity fading.

Reversible vs. irreversible capacity losses.—To analyze the observed overpotential, which is a kinetic hindrance of the (de)lithiation process, a rate test with BOT and EOT samples was conducted to evaluate how much of the lost capacity can be recovered at very low C-rates. For a C-rate approaching zero in combination with a lithium anode, the increased NCM-811 impedance over cycling and the associated overpotential should become negligible and lead to a regain of the original capacity, except for the capacity loss which is caused by an irreversible loss of electrochemically active material. The capacity share due to the loss of active CAM would then be equal to $(C_{\text{BOT}} - C_{\text{EOT}})/C_{\text{BOT}}$ ($= \Delta C/C_{\text{BOT}}$) at a given C-rate, as the C-rate approaches zero. The scheme in Figure 7a shows why the relative values (i.e., the comparison of BOT and EOT) should be used in this analysis. It is based on the fact that the cycling conditions, including C-rate, potential cut-offs, and temperature, determine the actual capacity that can be extracted from the CAM and which for NCMs is always below the theoretical capacity of $\approx 280 \text{ mAh/g}_{\text{NCM}}$. Let us compare two scenarios where either 100% (case A, e.g., with a very high cut-off voltage) or only 50% (case B, e.g., with an intermediate cut-off voltage) of the NCM capacity is accessed at BOT (i.e., in the absence of any loss of active material). The absolute capacity loss caused by an inactive surface layer (of the same thickness) at EOT will definitely be different for the two cases, meaning that the absolute loss for case B would only be half compared to that for case A (i.e., $\Delta C_B = 0.5 \cdot \Delta C_A$). In contrast, the BOT-normalized relative capacity loss is the same in both cases (i.e., $\Delta C/C_{\text{BOT}}$ would be identical) and is thus the correct measure for the loss of active material. However, as stated above, to quantify the irreversible capacity loss due to cyclable material loss

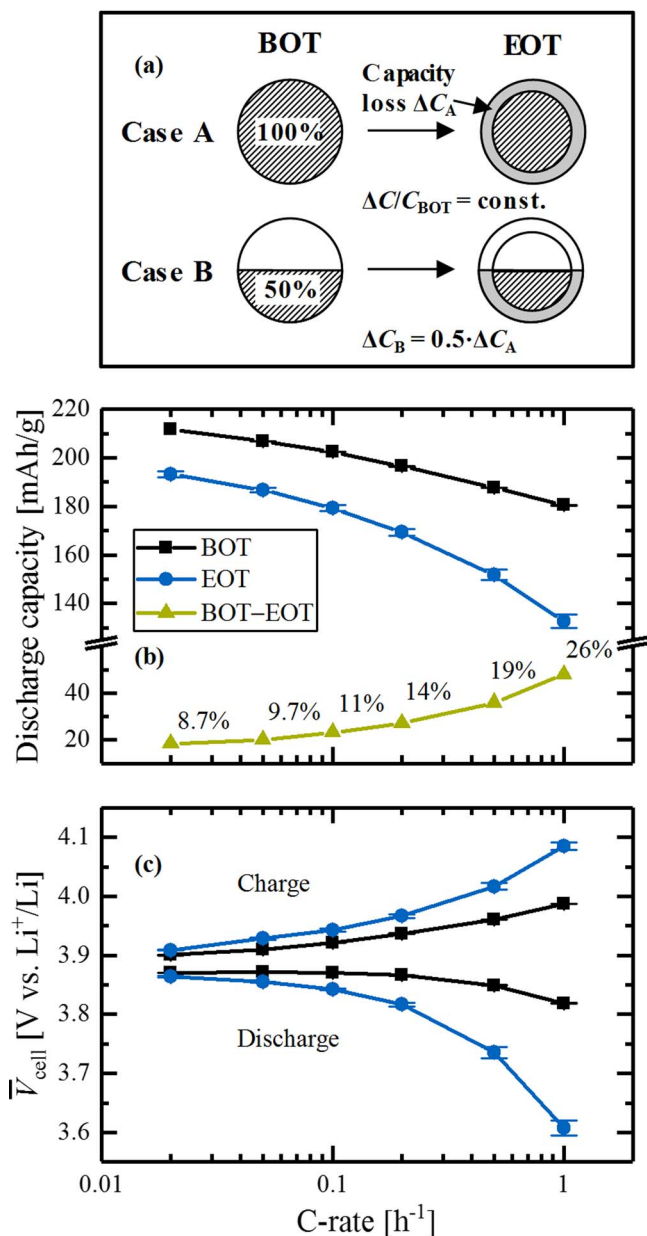


Figure 7. Rate test of BOT (i.e., test started after 18 regular cycles of the LDE protocol) and EOT NCM-811 cathodes harvested from cell 1 and 2, measured in a NCM-811/lithium coin-cell setup at 25°C. (a) Scheme illustrating the difference between absolute and relative capacity loss caused by an inactive phase. (b) Discharge capacities at BOT and EOT as well as their difference; the percentages marked on the latter are the difference between BOT and EOT capacity normalized to the BOT discharge capacity at the respective C-rate. (c) Mean charge and discharge cell voltages (\bar{V}_{cell}) of the NCM-811/Li cells. For EOT samples, the average capacity and \bar{V}_{cell} values for the NCM-811 cathodes harvested from cell 1 and cell 2 of the long-duration experiment are shown (error bars are min/max values); for the BOT samples, two nominally identical cells were measured.

by these means, the C-rate must be small enough so that overpotentials play no role anymore. This condition should be satisfied once the charge-averaged mean charge and discharge voltages (\bar{V}_{cell}) for NCM-811 cathodes harvested at EOT start to become sufficiently close to that of the BOT cells. In Figure 7c, this recovery of \bar{V}_{cell} during charge and discharge for the EOT cells (blue curve) is compared to the BOT cell (black curve) as the C-rate is decreased from 1C to C/50, reaching essentially identical \bar{V}_{cell} values for BOT and EOT cells at C/50 (less than 10 mV difference).

The effect of a decreasing overpotential with decreasing C-rate on the discharge capacity is shown in Figure 7b. Comparing the performance of the BOT (black curve) and EOT NCM-811 cathodes (blue curve) indicates that a large fraction of the discharge capacity is regained for the EOT cells by applying a slow cycling rate of C/50. In the light of our previous analysis, the remaining (irreversible) capacity loss should arise from the NCM-811 fraction that is lost to a reconstructed and electrochemically inactive surface layer. Thus, the irreversible capacity loss of ≈ 18 mAh/g at C/50 (green symbols in Figure 7b) that translates into a loss of cyclable material of 8.7% (from $\Delta C/C_{BOT}$) has to be compared to the relative material loss of 8.5%, which we calculated from the XPD analysis in Figure 5c. Considering the errors, which might occur in the XPD analysis (e.g., accuracy of the calibration curves) and the rate test (e.g., weighing error of the EOT electrodes, mean voltages even at C/50 not perfectly identical), the estimates for the loss of cyclable material are reasonably close and consistent. Summarizing the presented findings: The share of the electrochemically inactive material at EOT can be calculated from both our XPD analysis and the rate test, whereby the respective reference state has to feature the same overpotential and thus the same Δx_{Li} range as at end-of-test. At a rate of C/50 at which the overpotential is minor, this reference state is the begin-of-test, whereas the overpotential build-up at C/2 during long-term cycling is significant and only the theoretical XPD capacity of the same cycle (EOT in this case) can be used as reference state (see Equations 5 and 7).

Nature of the surface layer.—XPS measurements were conducted with pristine NCM-811 electrodes as well as harvested BOT and EOT NCM-811 cathode samples to further clarify the nature of the resistive surface layer. In order to ensure a comparable SOC between the pristine and cycled electrodes (as close as possible to 0%), the latter were regularly discharged to 3.0 V vs. Li⁺/Li, followed by constant voltage hold step with a C/100 current cut-off. Figure 8 is a zoom of the low-binding energy region of the O1s spectrum of pristine and aged NCM-811 samples (for the complete O1s spectrum and the used fitting parameters see Figure S10 and Table S11 in paragraph S6 of the SI). The O1s spectrum of the pristine sample shown in Figure 8a suggests the presence of a pure layered oxide with an O1s binding energy of 529.3 eV (indicated by the green line), similar to a different study conducted at our instrument.⁷² After 18 charge/discharge cycles, the spectrum already shows some intensity at energies higher than the layered oxide binding energy (529.9 eV, indicated by the blue line in Figure 8b), which can be attributed to an oxygen-deficient surface layer (blue marked area). The correlation between a shift to higher binding energies and oxygen depletion in surface-near regions is established based on reference spectra of layered MnO₂, spinel Mn₃O₄, and rock-salt MnO (see paragraph S6 in the SI). It is shown there, that the O-depleted Mn-samples, i.e., spinel and rocksalt, show a peak at 0.3–0.4 eV higher energy than the layered MnO₂. After 1000 cycles (Figure 8c), the intensity of the low binding energy O1s peak shifts considerably to higher binding energy, indicating a considerable oxygen depletion at the NCM-811 surface. Therefore, at least qualitatively, the XPS analysis supports our above hypothesis that an oxygen-depleted layer is formed upon extended cycling of NCM-811 between 3.0–4.5 V vs. Li⁺/Li.

Effect of the O-depleted surface layer on the SOC distribution.—Our XPD analysis showed that neither bulk structural changes, nor significant Ni-Li disorder are observable in NCM-811 over 1000 cycles (see Table I and Figure 3). However, a detailed analysis of the capacity losses indicates a loss of electrochemically active CAM (Figure 5), while the XPS analysis suggests that an oxygen-depleted surface film on the NCM-811 particles is formed upon cycling (Figure 8). Impedance data (Figure 6b) as well as rate tests (Figure 7) suggest an increased charge-transfer resistance, which is presumably caused by a resistive surface film. This poses the question whether a resistive surface layer is being formed on the external surface of each secondary NCM-811 particle with diameters of ≈ 5 –10 μm (see Figure S11 in paragraph S8 of the SI) or whether it is being formed around each of the

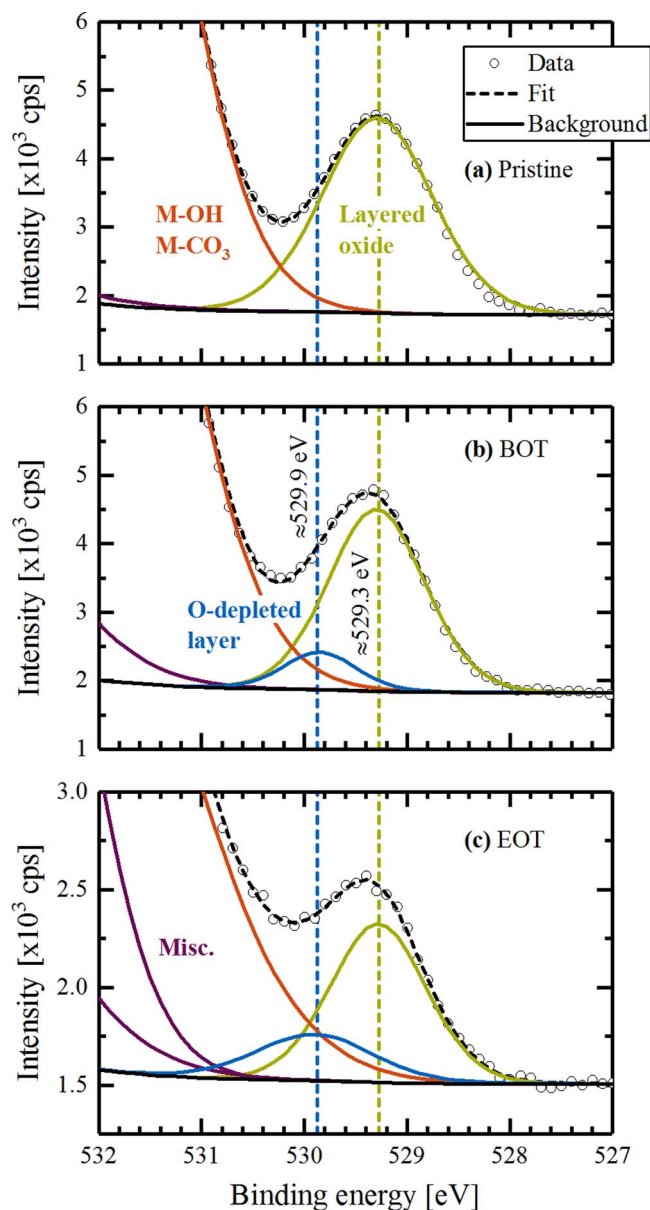


Figure 8. XPS O1s spectra of (a) pristine NCM-811 powder and of NCM-811 electrodes harvested at (b) BOT and (c) EOT. The binding energies of the layered oxide (green line) and an O-depleted surface layer (highlighted in blue) were inferred from MnO_2 , Mn_3O_4 , and MnO reference samples (see SI S6). Surface contaminants (hydroxides and carbonates) are fitted with one peak at higher binding energies (red line). The purple peaks referred to as miscellaneous (misc.) originate from organic surface impurities. For details on the XPS analysis and fitting procedure see paragraph S6 in the SI.

primary particles ($\approx 0.5\text{--}1\ \mu\text{m}$ in size) of which the secondary particle is composed. These two scenarios are sketched into the SEM cross-section image of a secondary NCM-811 particle shown in Figure 9a. As will be explained in the following, we will seek to examine these two scenarios by an operando XPD relaxation experiment, where the lattice parameter c is monitored upon the transition from a $C/2$ charge to OCV.

With an operando XPD relaxation experiment, the inhomogeneity of the lithium distribution (i.e., of x_{Li}) over the fresh NCM-811 electrode (after 9 cycles) and harvested EOT NCM-811 samples is compared. Thereby, the full width at half maximum (FWHM) of the reflections correlates with the homogeneity of the lattice spacing, meaning that a broader d -spacing distribution leads to a larger FWHM, whereas a homogenous d -spacing results in a sharp peak shape. Be-

cause the lattice parameters are closely linked to the lithium content x_{Li} in the NCM-811 material, the FWHM is a measure of the inhomogeneity of the SOC distribution. In this experiment, relative differences between the FWHMs of fresh and EOT samples are compared, wherefore the instrumental contribution to the broadening can be neglected (since the instrument provides a constant offset). In the relaxation experiment, selected reflections of the NCM-811 phase were monitored during the OCV period after a $C/2$ charge to a comparable SOC, as determined by the respective OCV (cut-off voltage of 4.3 V for fresh and 4.5 V for EOT NCM-811). The resulting OCV relaxation is shown in Figure 9b, whereby the initial potential drop from 4.3 V (fresh sample) and 4.5 V (EOT sample) to below 4.3 V occurred within the first 10 s of the OCV period. The final OCV of the fresh sample ($\approx 4.25\ \text{V}$ vs. Li^+/Li) is reasonably close to that of the EOT sample ($\approx 4.23\ \text{V}$ vs. Li^+/Li), indicating that indeed a very similar lithium content x_{Li} was established by the preceding charge at $C/2$. At such high SOCs (corresponding to OCV values higher than 4.2 V), the lattice parameter a is virtually constant, while the lattice parameter c depends very strongly on x_{Li} in this region (see Figure S6 in the SI). Therefore, in order to minimize the XPD data acquisition time, only the 003 reflection, which uniquely describes the lattice parameter c , was recorded for the data shown in Figure 9. This resulted in an acquisition time for the relevant 2θ region of ≈ 4 minutes (see Experimental section). Analogous relaxation measurements recording both the (110) and the (003) reflection (≈ 8 minutes acquisition time) were also recorded to verify that the a parameter indeed remains essentially constant during the OCV transients (data not shown).

As can be seen in Figure 9c, the lattice parameter c exhibits a slight increase during the OCV phase. In the case of the EOT sample, this could be attributed to relaxation processes within the NCM-811 material, meaning the distribution of Li ions across the bulk of the NCM-811 structure, because the FWHM (Figure 9d) also indicates such a relaxation process. Assuming a constant a value of $\approx 2.815\ \text{\AA}$ during relaxation (estimation based on data shown in Figure S6 in the SI), the SOC change can be calculated from the c/a change and the high-SOC calibration curve (shown in Figure 5a). Thus, the observed relaxation of the lattice parameter c for the EOT sample correlates to $\Delta x_{\text{Li}} \approx 0.015$ and $\Delta \text{SOC} \approx 4.1\ \text{mAh/g}$ (vs. $\Delta x_{\text{Li}} \approx 0.009$ and $\Delta \text{SOC} \approx 2.4\ \text{mAh/g}$ for the fresh sample). Both values show that the net capacity change during the OCV period is minor. For the fresh sample however, this process cannot be correlated to the equilibration of an initially inhomogeneous SOC distribution across the bulk of NCM-811 particles, because in this case no relaxation of the FWHM is observed. Currently, we cannot provide a solid explanation for the apparent re-lithiation of the material. One hypothesis is that electrolyte oxidation (possibly also triggered by the permanent X-ray beam) might lead to a small re-lithiation of the CAM, as suggested by Xia et al.⁷³ It is important to note here that the XPD data collection during the LDE study was usually performed after a 3–5 h long OCV phase, meaning that the LDE XPD data are expected to depict a well-equilibrated state.

From the FWHM of the reflections, conclusions on the heterogeneity of the lattice spacing can be drawn. Assuming a virtually constant a parameter, a broader FWHM of the (003) reflection thereby translates into a more pronounced inhomogeneity of the Li distribution within the NCM-811 particles. For a fresh material, no relaxation process can be seen for the FWHM (black symbols/curve in Figure 9d), and the OCV relaxation is rather small ($\approx 30\ \text{mV}$ between $\approx 5\ \text{s}$ and $\approx 5\ \text{h}$ into the OCV period, black curve in Figure 9b; initial voltage drop of $\approx 20\ \text{mV}$ within the first 5 s not shown here), which we believe is due to both the relaxation of concentration gradients within the electrolyte phase and the above discussed slight extent of re-lithiation. In contrast, the EOT sample shows a significantly larger decrease in both OCV ($\approx 50\ \text{mV}$ between $\approx 10\ \text{s}$ and $\approx 5\ \text{h}$ into the OCV period, blue curve in Figure 9b; initial voltage drop of $\approx 220\ \text{mV}$ in the first 10 s not shown here) and FWHM curves (blue symbols/curve in Figure 9d). The initial FWHM for the EOT NCM-811 is more than double compared to that of the fresh cathode material, indicating a severe d -spacing heterogeneity in the c direction. The final FWHM value after relaxation is the same for both samples, suggesting that an equally homogeneous Li distribution

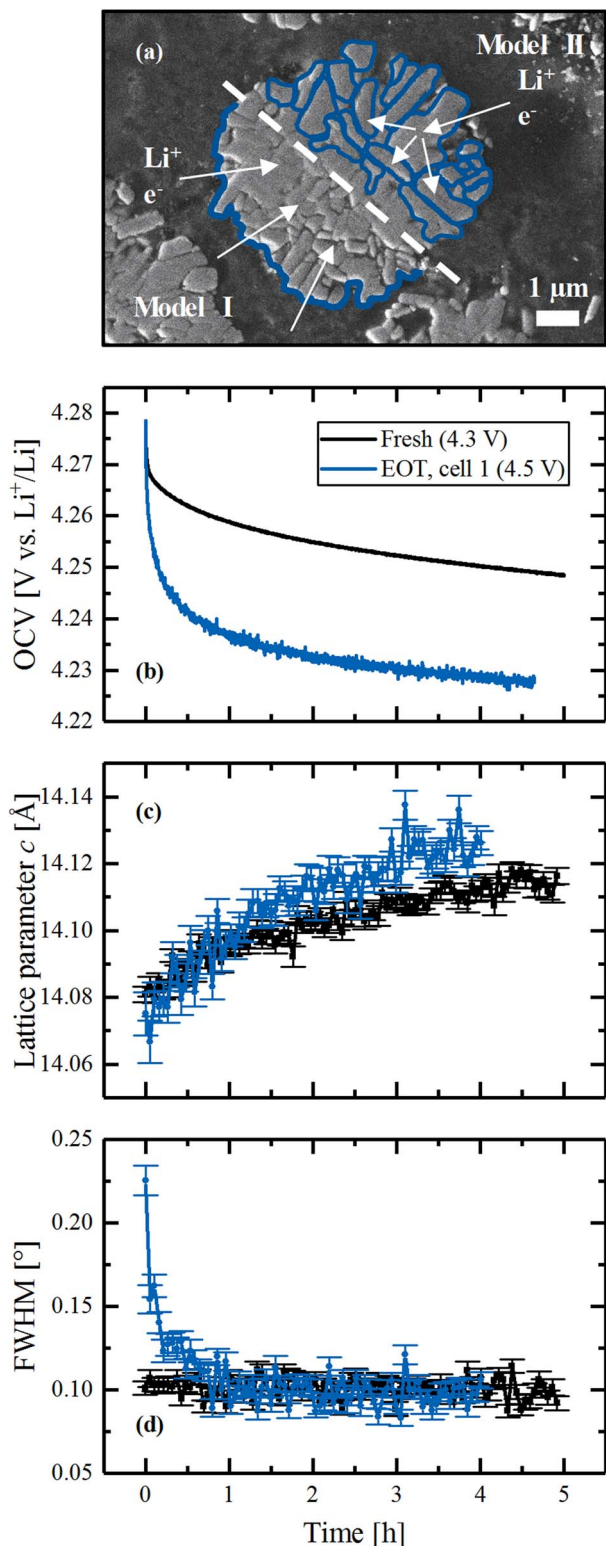


Figure 9. (a) SEM image of an NCM-811 particle, with a scheme illustrating the two discussed models for the formation of the O-deficient surface layer (sketched in blue): (i) either around the external surface of the secondary agglomerates (model I) or (ii) around each individual primary particle (model II). (b-d) Operando L-XPD relaxation experiment at the in-house diffractometer with fresh (measured in the 9th cycle, black curve) and EOT NCM-811 samples (from cell 1, blue curve) after charging to a comparable SOC with C/2: Evolution of (b) the NCM-811 cathode OCV, (c) the lattice parameter *c* determined from the (003) reflection, and (d) the FWHM of the (003) reflection during OCV period. The XPD data were acquired with a time resolution of ≈ 4 minutes.

across the bulk of the NCM-811 particles can be achieved in the EOT sample after prolonged relaxation times. This is another strong support for our above conclusion that the bulk structure of the NCM-811 material is not significantly altered by cycling over 1000 cycles.

On the other hand, the observed FWHM relaxation behavior for the EOT sample could in principle have several causes: (i) an inhomogeneous degree of NCM-811 delithiation across the cathode thickness, if the ionic resistance within the electrolyte phase (R_{ion}) were sufficiently large; (ii) an inhomogeneous lithium distribution within the bulk phase of each of the primary particles due to hindered lithium diffusion in the solid phase; and/or, (iii) different degrees of delithiation within the secondary particles.¹³ Despite the increase of the ionic resistance over cycling (from initially $R_{\text{ion}} \approx 3 \Omega \text{ cm}^2$ to $R_{\text{ion}} \approx 9 \Omega \text{ cm}^2$ after 1000 cycles; see paragraph S4 in the SI), the absolute potential drop at C/2 due to R_{ion} is only ≈ 7 mV even after 1000 cycles, which would imply an essentially homogeneous delithiation across the cathode thickness upon charge, so that the first possible cause (i) should be negligible. With regards to the second possible cause (ii), our XPD analysis clearly indicates that there is no significant change in the Li-Ni disorder over 1000 cycles, so that one would not expect any differences in the lithium diffusion within the NCM-811 bulk phase between fresh and EOT NCM-811. This leaves the third possible cause (iii) as an explanation for the slow FWHM relaxation of the EOT NCM-811, namely an uneven degree of delithiation within the secondary particles. This must be due to the formation of the O-depleted surface layer upon cycling. Addressing our initial question, this surface layer can either be formed around (i) the secondary particles (model I in Figure 9a, sketched by the blue lines) or (ii) around the primary particles (model II) which agglomerate to the former.

For the first scenario (model I), the poor lithium ion conductivity through the resistive layer (as suggested by the large increase in R_{CT} upon cycling, see Figure 6b) around the secondary particle would be rate determining. After overcoming this barrier, the SOC distribution in the primary particles within each secondary particle would be homogeneous, in which case no initial broadening of the FWHM recorded during the OCV period following the C/2 charge would be expected for the EOT sample, contrary to what is observed in Figure 9d. For the other scenario (model II) with a resistive surface layer formed around every primary particle within a secondary particle, a homogenous degree of delithiation would also be expected within a given primary particle, but assuming that the transport of lithium ions and/or electrons is hindered by the surface film and must proceed through the NCM-811 solid phase, the degree of delithiation would be lower for primary particles deeper within the secondary particle compared to those at its outer surface. This would correspond to a SOC variation between primary particles, which would result in an initially broad FWHM in the OCV period following the C/2 charge. Over an extended OCV period, an equilibration of the different SOCs of the primary particles within a secondary particle would occur, so that the FWHM should ultimately narrow to the value observed for a fresh NCM-811 sample. This is exactly what is observed during relaxation of the EOT NCM-811 sample (see Figure 9d). Therefore, on the basis of this analysis of the operando L-XPD relaxation experiment, strong evidence is provided that the resistive O-depleted surface layer must be forming around primary particles in the cycled NCM-811 CAM.

Quite clearly, an aging mechanism according to model II is most consistent with our experimental observation so far. However, the question remains whether the delithiation of the primary particles toward the center of the secondary particles is limited by the transport of Li-ions or of electrons. Seeking to examine this question, the particle morphology of pristine and discharged EOT NCM-811 samples was analyzed by SEM, hoping that it might answer the extent of particle cracking (see paragraph S8 in the SI). Interestingly, the particle morphology at BOT compared to that at EOT shows no significant difference, indicating that NCM-811 particles are not cracked into clearly separate pieces over the 1000 cycles. However, it needs to be stressed out here that the samples were mechanically polished to obtain cross-sectional SEM images, which renders it impossible to differentiate

between small cracks and grain boundaries that are present even in the pristine NCM-811 CAM.

The formation of cracks, however, can also be examined by Kr-BET surface area measurements, as cracks would have to lead to an increase in the specific surface area. The pristine NCM-811 powder has a BET surface area of $\approx 0.28 \text{ m}^2/\text{g}$, which for non-porous spherical particles would predict a particle diameter of $\approx 4.5 \text{ }\mu\text{m}$ (see equation (S11) in paragraph S7 of the SI). This is reasonably consistent with the secondary particle size observed by SEM (see Figure S11 in paragraph S8 of the SI), suggesting that essentially only the external surface of the pristine NCM-811 would be accessible to the electrolyte. However, it may be the case that there are simply surface impurities on the external surfaces of the secondary and/or primary particles (e.g., Li_2CO_3 or LiOH), which prevent gas (and electrolyte) access to within the secondary particles. Therefore, as these could be removed during cycling,⁵⁶ or by protons/HF formed during (electro)chemical electrolyte oxidation,^{74,75} we conducted two more Kr-BET measurements to mimic this conditions in a real cell. NCM-811 was treated either with (i) water for 30 min or (ii) over a period of 7 days with LP57 electrolyte containing $\approx 2000 \text{ ppm HF}$ (see Experimental section). After these treatments, the BET surface area has increased by ≈ 4 -fold to $\approx 1.2 \text{ m}^2/\text{g}$ in both cases. For the solid sphere approximation, this would correspond to a particle diameter of $\approx 1 \text{ }\mu\text{m}$, which is on the order of the dimensions of the primary particles (see Figure S11), indicating that the pores within the thus treated secondary NCM-811 particles become accessible for gas adsorption. Considering the known formation of protons/HF during (electro)chemical oxidation,⁷⁵ which is expected to be substantial over extensive cycling of NCM-811 to potentials of 4.5 V vs. Li^+/Li , one would also expect that the surface of the primary particles within the secondary particles gradually becomes accessible to the electrolyte over the course of cycling. The fact that the primary particles shrink by up to $\approx 6\%$ when NCM-811 is charged to 4.5 V vs. Li^+/Li (see unit cell volume change in Figure S6) provides an additional argument for the electrolyte penetration into pores during cycling.

These pores would enable the release of O_2 gas from inside the secondary particles, thereby enabling the formation of an O-depleted resistive surface layer on the primary particles, ultimately leading to the morphology termed as model II in Figure 9a. The limiting transport mechanism, which leads to the initial broadening of the FWHM observed for the EOT NCM-811 sample during the OCV relaxation experiment (Figure 9d), would thus have to be due to a poor electronic conduction pathway into the aged secondary NCM-811 particle (across now loosely connected primary particles covered by a resistive O-depleted film), as a relatively fast lithium ion transport could proceed through the electrolyte within the pores.

In summary, while many literature reports claim that particle cracking is a major degradation process in NCM cathodes,^{12–14} our analysis suggests that it is rather the interplay of cracks formed due to structural changes during cycling in conjunction with the dissolution of surface impurities that gradually increase the specific surface area of NCMs. As this goes along with an increasing accessibility of the electrolyte to the primary particles in the interior of the secondary particles, an O-depleted resistive surface layer can be formed on the primary particles, which in turns leads to the observed capacity fading. Based on the here proposed aging mechanism, the cycling stability of single-crystal NCMs would be predicted to be superior to poly-crystalline materials.

Estimated thickness of the O-depleted surface layer.—Assuming that the BET surface area of $1.2 \text{ m}^2/\text{g}$ for the washed or HF-treated NCM-811 is representative for NCM-811 after 1000 cycles, the thickness of the O-depleted surface could be estimated by a similar approach as described in literature (for the calculation see paragraph S7 in the SI).^{16,57} Assuming a solid sphere, a primary particle size of $\approx 1 \text{ }\mu\text{m}$ is obtained, which is in good agreement with what can be seen in the SEM images (Figure 9a and paragraph S8 in the SI). The material loss of $\approx 8.5\%$ from the XPD analysis in Figure 5c equals to the phase fraction of the O-depleted surface layer, which translates to a layer thickness of $\approx 15 \text{ nm}$. This is in good agreement with literature values, which

also include transmission electron microscopy images.^{67,76} Watanabe et al.⁷⁶ cycled NCA full-cells to 4.2 V for 1000 cycles and found a $\approx 8 \text{ nm}$ thick NiO-like surface layer at 25°C (and $\approx 25 \text{ nm}$ at 60°C), supporting our model of a surface reconstruction around primary particles. Jung et al.⁶⁷ performed half-cell cycling with NCM-523 cathodes to upper cut-off voltages of 4.5 V and 4.8 V vs. Li^+/Li , respectively, observing a gradual surface transformation from layered via spinel to rock-salt structure, with a layer thickness of $\approx 15\text{--}20 \text{ nm}$, depending on the cut-off voltage. Note, that in Figure 9a, the surface layer of model I is depicted thicker to stress that in this case, based on a smaller BET surface area of $0.28 \text{ m}^2/\text{g}$, the layer thickness would be around $\approx 66 \text{ nm}$, which is much thicker than the typical values reported in the literature, providing further support for model II shown in Figure 9a. We finally tried to validate the layer thickness from cross-sectional HAADF-STEM images of pristine, BOT, and EOT samples, which were prepared by focused ion beam milling (for details and images see paragraph S9 in the SI). While the pristine CAM exhibits no defects at the surface, proving its purely layered nature, transition-metals partially occupy the inter-slabs in the surface-near region of the BOT and EOT samples, as it would be the case for the spinel and/or rock-salt structure. The disordered surface layer was identified on numerous of the primary NCM-811 particles, but it was not possible to accurately quantify the surface layer thicknesses due to several reasons: (i) in many cases, the primary particles could not be tilted into the desired low-indexed zone axes, and, (ii) no clear boundary could be observed between the different phases, as they probably merge gradually into each other.⁶⁷

Conclusions

In this work, we investigated the capacity fading in NCM-811/graphite full-cells over 1000 cycles, whereby focusing on the cathode by pre-lithiating the anode, to identify fading mechanisms with a combination of diagnostics, such as in situ and operando XPD, EIS, and XPS. From an ex situ XPD refinement of the NCM-811 before and after 1000 cycles, we concluded the bulk stability of the CAM with an unaltered Ni-Li disorder of $\approx 3\%$. Based on data from in situ XPD analysis, we were able to establish a quantitative correlation between lattice parameter changes and capacity losses in NCM-811 over the course of cycling. We concluded that the thereby identified capacity losses are caused by a shrinkage of the effective SOC window at both low and high SOC due to an increased cathode polarization. This overpotential build-up was further confirmed by cathode EIS measurements using a gold wire micro-reference electrode showing a 10-fold increase of the charge-transfer resistance. Furthermore, the difference between the capacity loss predicted by the in situ XPD analysis and that obtained from the electrochemical data reveals a CAM loss of $\approx 8.5\%$. These observations are consistent with the formation of an O-depleted resistive surface layer, which was found by XPS measurements and is assumed to show no Li intercalation. An operando XPD relaxation experiment leads us to conclude that the impedance build-up across a secondary particle is caused by the formation of a resistive O-depleted surface layer around the individual primary particles. This conclusion is further supported by BET measurements and cross-sectional SEM as well as HAADF-STEM pictures. The observed surface reconstruction on the one hand means a loss of CAM, which results in an irreversible capacity loss. On the other hand, it causes a significant overpotential thereby shrinking the apparent SOC window. This reversible capacity loss could be regained at very low C-rates. To avoid a surface reconstruction, less resistive and protective coatings for Ni-rich CAMs are essential to improve capacity retention and cycle life in future LIBs.

Acknowledgments

Financial support by BASF SE through its Scientific Network on Electrochemistry and Batteries is gratefully acknowledged. We also wish to acknowledge the Diamond Light Source for provision of beamtime at the Beamline I11 (proposal EE16866) and financial support. Further gratitude is expressed to Sophie Solchenbach for her con-

tribution to the impedance measurements, to Katia Rodewald from the Wacker-Chair of Macromolecular Chemistry at the Technical University of Munich for the SEM measurements, and to the Competence Center Material Physics of BASF SE for the STEM measurements.

ORCID

Franziska Friedrich  <https://orcid.org/0000-0001-9400-1212>

Benjamin Strehle  <https://orcid.org/0000-0001-8878-1160>

Michele Piana  <https://orcid.org/0000-0002-3310-6587>

References

- Pedro Lima, Pushevs, can be found under <https://pushevs.com/2018/04/05/samsung-sdi-94-ah-battery-cell-full-specifications>, accessed October 2019.
- E. A. Olivetti, G. Ceder, G. G. Gaustad, and X. Fu, *Joule*, **1**, 229 (2017).
- A. H. Tkaczyk, A. Bartl, A. Amato, V. Lapkovskis, and M. Petranikova, *J. Phys. D Appl. Phys.*, **51**, 203001 (2018).
- C. B. L. Nkulu, L. Casas, V. Haufroid, T. De Putter, N. D. Saenen, T. Kayembe-Kitenge, P. M. Obadia, D. K. W. Mukoma, J.-M. L. Ilunga, T. S. Nawrot, O. L. Numbi, E. Smolders, and B. Nemery, *Nat. Sustain.*, **1**, 495 (2018).
- M. H. Kim, H. S. Shin, D. Shin, and Y. K. Sun, *J. Power Sources*, **159**, 1328 (2006).
- T. Ohzuku, A. Ueda, and M. Nagayama, *J. Electrochem. Soc.*, **140**, 1862 (1993).
- H. Li, N. Zhang, J. Li, and J. R. Dahn, *J. Electrochem. Soc.*, **165**, A2985 (2018).
- W. Li, J. Reimers, and J. Dahn, *Solid State Ionics*, **67**, 123 (1993).
- H. Arai, S. Okada, H. Ohtsuka, M. Ichimura, and J. Yamaki, *Solid State Ionics*, **80**, 261 (1995).
- J.-M. Kim and H.-T. Chung, *Electrochim. Acta*, **49**, 3573 (2004).
- W. Li, X. Liu, H. Celio, P. Smith, A. Dolocan, M. Chi, and A. Manthiram, *Adv. Energy Mater.*, **8**, 1703154 (2018).
- K. Ishidzu, Y. Oka, and T. Nakamura, *Solid State Ionics*, **288**, 176 (2016).
- H. Liu, M. Wolf, K. Karki, Y.-S. Yu, E. A. Stach, J. Cabana, K. W. Chapman, and P. J. Chupas, *Nano Lett.*, **17**, 3452 (2017).
- E. J. Lee, Z. Chen, H.-J. Noh, S. C. Nam, S. Kang, D. H. Kim, K. Amine, and Y.-K. Sun, *Nano Lett.*, **14**, 4873 (2014).
- R. Jung, M. Metzger, F. Maglia, C. Stinner, and H. A. Gasteiger, *J. Electrochem. Soc.*, **164**, A1361 (2017).
- B. Strehle, K. Kleiner, R. Jung, F. Chesneau, M. Mendez, H. A. Gasteiger, and M. Piana, *J. Electrochem. Soc.*, **164**, A400 (2017).
- T. Teufl, B. Strehle, P. Müller, H. A. Gasteiger, and M. A. Mendez, *J. Electrochem. Soc.*, **165**, A2718 (2018).
- D. Streich, C. Erk, A. Guéguen, P. Müller, F.-F. Chesneau, and E. J. Berg, *J. Phys. Chem. C*, **121**, 13481 (2017).
- F. Lin, I. M. Markus, D. Nordlund, T. C. Weng, M. D. Asta, H. L. Xin, and M. M. Dieff, *Nat. Commun.*, **5**, 3529 (2014).
- S. Sallis, N. Pereira, P. Mukherjee, N. F. Quackenbush, N. Faenza, C. Schlueter, T. L. Lee, W. L. Yang, F. Cosandey, G. G. Amatucci, and L. F. Piper, *J. Appl. Phys. Lett.*, **108**, 263902 (2016).
- H. Zheng, Q. Sun, G. Liu, X. Song, and V. S. Battaglia, *J. Power Sources*, **207**, 134 (2012).
- K. Amine, Z. Chen, Z. Zhang, J. Liu, W. Lu, Y. Qin, J. Lu, L. Curtis, and Y.-K. Sun, *J. Mater. Chem.*, **21**, 17754 (2011).
- S. Solchenbach, G. Hong, A. T. S. Freiberg, R. Jung, and H. A. Gasteiger, *J. Electrochem. Soc.*, **165**, 3304 (2018).
- USABC, USABC Goals for Advanced Batteries for EVs - CY2020 Commercialization, can be found under https://www.energy.gov/sites/prod/files/2014/05/f15/APR13_Energy_Storage_d_III_Adv_Battery_Dev_0.pdf, accessed October 2019.
- D. Andre, S. Kim, P. Lamp, F. Lux, and F. Maglia, *J. Mater. Chem. A Mater. Energy Sustain.*, **3**, 6709 (2015).
- K. Kleiner, B. Strehle, A. R. Baker, S. J. Day, C. C. Tang, I. Buchberger, F.-F. Chesneau, H. A. Gasteiger, and M. Piana, *Chem. Mater.*, **30**, 3656 (2018).
- C. A. Murray, J. Potter, S. J. Day, A. R. Baker, S. P. Thompson, J. Kelly, C. G. Morris, S. Yang, and C. C. Tang, *J. Appl. Crystallogr.*, **50**, 172 (2017).
- M. Basham, J. Filik, M. T. Wharmby, P. C. Y. Chang, B. El Kassaby, M. Gerring, J. Aishima, K. Levik, B. C. A. Pulford, I. Siharulidze, D. Sneddon, M. Webber, S. S. Dhesi, F. Maccherozzi, O. Svensson, S. Brockhauser, G. Náray, and A. W. Ashton, *J. Synchrotron Radiat.*, **22**, 853 (2015).
- J. Filik, A. W. Ashton, P. C. Y. Chang, S. J. Day, M. Drakopoulos, M. W. Gerring, M. L. Hart, O. V. Magdysyuk, S. Michalik, A. Smith, C. C. Tang, N. J. Terril, M. T. Wharmby, and H. Wilhelm, *J. Appl. Crystallogr.*, **50**, 959 (2017).
- A. Coelho, Coelho Software (2016).
- O. Dolotko, A. Senyshyn, M. J. Mühlbauer, K. Nikolowski, and H. Ehrenberg, *J. Power Sources*, **255**, 197 (2014).
- S. H. Bo, K.-W. Nam, O. J. Borkiewicz, Y.-Y. Hu, X.-Q. Yang, P. J. Chupas, K. W. Chapman, L. Wu, L. Zhang, F. Wang, C. P. Grey, and P. G. Khalifah, *Inorg. Chem.*, **53**, 6585 (2014).
- T. A. Hewstone and B. L. Chamberland, *J. Phys. Chem. Solids*, **48**, 97 (1987).
- H. Liu, H. Liu, S. H. Lapidus, Y. S. Meng, P. J. Chupas, and K. W. Chapman, *J. Electrochem. Soc.*, **164**, A1802 (2017).
- Y. Arachi, H. Kobayashi, S. Emura, Y. Nakata, M. Tanaka, T. Asai, H. Sakaebe, K. Tatsumi, and H. Kageyama, *Solid State Ionics*, **176**, 895 (2005).
- O. Sekizawa, T. Hasegawa, N. Kitamura, and Y. Idemoto, *J. Power Sources*, **196**, 6651 (2011).
- Y. J. Gu, Y. B. chen, H. Q. Liu, Y. M. Wang, C. L. Wang, and H. K. Wu, *J. Alloys Compd.*, **509**, 7915 (2011).
- M. Ma, N. A. Chernova, B. H. Toby, P. Y. Zavalij, and M. S. Whittingham, *J. Power Sources*, **165**, 517 (2007).
- P. Whitfield, I. Davidson, L. Cranswick, I. Swainson, and P. Stephens, *Solid State Ionics*, **176**, 463 (2005).
- A. Hirano, K. Kanie, T. Ichikawa, N. Imanishi, Y. Takeda, R. Kanno, T. Kamiyama, and F. Izumi, *Solid State Ionics*, **152–153**, 207 (2002).
- L. Yin, G. S. Mattei, Z. Li, J. Zheng, W. Zhao, F. Omenya, C. Fang, W. Li, J. Li, Q. Xie, J.-G. Zhang, M. S. Whittingham, Y. S. Meng, A. Manthiram, and P. G. Khalifah, *Rev. Sci. Instrum.*, **89**, 093002 (2018).
- S. Sasaki, K. Fujino, and Y. Takéuchi, *Proc. Japan Acad. Ser. B Phys. Biol. Sci.*, **55**, 43 (1979).
- S. Sasaki, K. Fujino, Y. Takéuchi, and R. Sadanaga, *Acta Crystallogr. Sect. A*, **36**, 904 (1980).
- P. W. Stephens, *J. Appl. Crystallogr.*, **32**, 281 (1999).
- A. O. Kondrakov, H. Geßwein, K. Galdina, L. de Biasi, V. Meded, E. O. Filatova, G. Schumacher, W. Wenzel, P. Hartmann, T. Brezesinski, and J. Janek, *J. Phys. Chem. C*, **121**, 24381 (2017).
- A. Senyshyn, O. Dolotko, M. J. Mühlbauer, K. Nikolowski, H. Fuess, and H. Ehrenberg, *J. Electrochem. Soc.*, **160**, A3198 (2013).
- O. Dolotko, A. Senyshyn, M. J. Mühlbauer, K. Nikolowski, F. Scheiba, and H. Ehrenberg, *J. Electrochem. Soc.*, **159**, A2082 (2012).
- S. Solchenbach, D. Pritzl, E. J. Y. Kong, J. Landesfeind, and H. A. Gasteiger, *J. Electrochem. Soc.*, **163**, A2265 (2016).
- J. Landesfeind, D. Pritzl, and H. A. Gasteiger, *J. Electrochem. Soc.*, **164**, A1773 (2017).
- D. Strmcnik, I. E. Castelli, J. G. Connell, D. Haering, M. Zorko, P. Martins, P. P. Lopes, B. Genorio, T. Østergaard, H. A. Gasteiger, F. Maglia, B. K. Antonopoulos, V. R. Stamenkovic, J. Rossmeisl, and N. M. Markovic, *Nat. Catal.*, **1**, 255 (2018).
- I. Buchberger, S. Seidlmayer, A. Pokharel, M. Piana, J. Hattendorff, P. Kudejova, R. Gilles, and H. A. Gasteiger, *J. Electrochem. Soc.*, **162**, A2737 (2015).
- J. Choi and A. Manthiram, *Solid State Ionics*, **176**, 2251 (2005).
- F. German, A. Hintennach, A. LaCroix, D. themig, S. Oswald, F. Scheiba, M. J. Hoffmann, and H. Ehrenberg, *J. Power Sources*, **264**, 100 (2014).
- S. H. Kang, D. P. Abraham, W. S. Yoon, K. W. Nam, and X. Q. Yang, *Electrochim. Acta*, **54**, 684 (2008).
- S. H. Kang, W. S. Yoon, K. W. Nam, X. Q. Yang, and D. P. Abraham, *J. Mater. Sci.*, **43**, 4701 (2008).
- R. Jung, R. Morasch, P. Karayaylali, K. Philips, F. Maglia, C. Stinner, Y. Shao-Horn, and H. A. Gasteiger, *J. Electrochem. Soc.*, **165**, A132 (2018).
- R. Jung, M. Metzger, F. Maglia, C. Stinner, and H. A. Gasteiger, *J. Phys. Chem. Lett.*, **8**, 4820 (2017).
- S.-K. Jung, H. Gwon, J. Hong, K.-Y. Park, D.-H. Seo, H. Kim, J. Hyun, W. Yang, and K. Kang, *Adv. Energy Mater.*, **4**, 1300787 (2014).
- Y. Makimura, T. Sasaki, T. Nonaka, Y. F. Nishimura, T. Uyama, C. Okuda, Y. Itou, and Y. Takeuchi, *J. Mater. Chem. A*, **4**, 8350 (2016).
- H. H. Ryu, K. J. Park, C. S. Yoon, and Y. K. Sun, *Chem. Mater.*, **30**, 1155 (2018).
- S. Choi and A. Manthiram, *J. Electrochem. Soc.*, **149**, A1157 (2002).
- H. R. Kim, S. G. Woo, J. H. Kim, W. Cho, and Y. J. Kim, *J. Electroanal. Chem.*, **782**, 168 (2016).
- S. Watanabe, T. Hosokawa, K. Morigaki, M. Kinoshita, and K. Nakura, *ECS Trans.*, **41**, 65 (2012).
- N. Yabuuchi, Y. Makimura, and T. Ohzuku, *J. Electrochem. Soc.*, **154**, A314 (2007).
- L. de Biasi, A. O. Kondrakov, H. Geßwein, T. Brezesinski, P. Hartmann, and J. Janek, *J. Phys. Chem. C*, **121**, 26163 (2017).
- A. O. Kondrakov, A. Schmidt, J. Xu, H. Geßwein, R. Mönig, P. Hartmann, H. Sommer, T. Brezesinski, and J. Janek, *J. Phys. Chem. C*, **121**, 3286 (2017).
- S. K. Jung, H. Gwon, J. Hong, K.-Y. Park, D.-H. Seo, H. Kim, J. Hyun, W. Yang, and K. Kang, *Adv. Energy Mater.*, **4**, 1300787 (2014).
- D. Mohanty, K. Dahlberg, D. M. King, L. A. David, A. S. Sefat, D. L. Wood, C. Daniel, S. Shar, V. Mahajan, M. Lee, and F. Albano, *Sci. Rep.*, **6**, 26532 (2016).
- K. Luo, M. R. Roberts, R. Hao, N. Guerrini, D. M. Pickup, Y.-S. Liu, K. Edström, J. Guo, A. V. Chadwick, L. C. Duda, and P. G. Bruce, *Nat. Chem.*, **8**, 684 (2016).
- T. Teufl, D. Pritzl, S. Solchenbach, H. A. Gasteiger, and M. A. Mendez, *J. Electrochem. Soc.*, **166**, A1275 (2019).
- H. Koga, L. Croguennec, M. Ménétrier, P. Mannesiez, F. Weill, and C. Delmas, *J. Power Sources*, **236**, 250 (2013).
- H. Sclar, J. Sicklinger, E. M. Ericson, S. Maiti, J. Grinblat, M. Talianker, L. Burstein, H. Beyer, G. Avruschenko, H. A. Gasteiger, B. Markovsky, and D. Aurbach, *to be submitted*.
- J. Xia, K. J. Nelson, Z. Lu, and J. R. Dahn, *J. Power Sources*, **329**, 387 (2016).
- M. Metzger, B. Strehle, S. Solchenbach, and H. A. Gasteiger, *J. Electrochem. Soc.*, **163**, 798 (2016).
- J. Wandt, A. T. S. Freiberg, A. Ogródnik, and H. A. Gasteiger, *Mater. Today*, **21**, 825 (2018).
- S. Watanabe, M. Kinoshita, T. Hosokawa, K. Morigaki, and K. Nakura, *J. Power Sources*, **258**, 210 (2014).